

CZECH TECHNICAL UNIVERSITY IN PRAGUE  
FACULTY OF NUCLEAR SCIENCES AND PHYSICAL ENGINEERING  
DEPARTMENT OF PHYSICS

Programme: Applied natural sciences  
Branch of Study: Physics and Technology of Nuclear Fusion



# Optimization of laser-accelerated ion beam divergence

## Optimalizace rozptylu iontových svazků urychlených laserem

MASTER'S THESIS

Author: Bc. Martina Žáková  
Supervisor: Ing. Jan Pšikal, PhD.  
Consultant: Dr. Daniele Margarone, PhD.  
Submitted in: May 2015

## **Prohlášení**

Prohlašuji, že jsem svou diplomovou práci vypracovala samostatně a použila jsem pouze podklady (literaturu, projekty, SW atd.) uvedené v příloženém seznamu.

Nemám závažný důvod proti použití tohoto školního díla ve smyslu § 60 Zákona č. 121/200 Sb., o právu autorském, o právech souvisejících s právem autorským a o změně některých zákonů (autorský zákon).

V Praze dne .....

.....

Bc. Martina Žáková

## **Acknowledgements**

I would like to thank my supervisor Ing. Jan Pšikal, PhD. and consultant Dr. Daniele Margarone, PhD. for providing expert advices, kind comments, willingness and friendly approach during this work.

*Název práce:*

**Optimalizace rozptylu iontových svazků urychlených laserem**

*Autor:* Bc. Martina Žáková

*Obor:* Fyzikální inženýrství

*Druh práce:* Diplomová práce

*Vedoucí práce:* Ing. Jan Pšikal, PhD.

Czech Technical University in Prague – Faculty of Nuclear Sciences and Physical Engineering (Department of Physical Electronics), ELI-Beamlines Project; Institute of Physics of the Academy of Sciences of the Czech Republic

*Konzultant:* Dr. Daniele Margarone, PhD.

ELI-Beamlines Project; Institute of Physics of the Academy of Sciences of the Czech Republic

*Abstrakt:* Hlavním cílem práce je teoretické studium urychlování iontů při interakci vysocevýkonných ultrakrátkých (femtosekundových) laserových impulzů s ionizovanými pevnými terči se zaměřením na úhlový rozptyl takto generovaných iontových svazků. Důležitou částí je studium omezení úhlového rozptylu těchto iontů, například pomocí tvaru terče nebo prostřednictvím magnetického pole solenoidu za terčem. Dle dosažených výsledků je divergence redukována nejlépe pomocí terče s výřezem na zadní straně a pomocí zahnutého terče. Dále je demonstrována schopnost magnetického solenoidu snížit divergenci protonového svazku určité energie až desetkrát oproti původní hodnotě. Ke studiu je využito dvou-dimenzionálních Particle-in-cell simulací a programu Matlab. Tato práce je důležitá pro realizaci a optimalizaci budoucích experimentů v rámci projektu ELI-Beamlines, ale i experimentů prováděných v institutu GIST v Gwangju, v Koreji.

*Klíčová slova:* divergence protonového svazku, laserem řízené iontové svazky, Particle-in-cell simulace, designově pokročilé terče, magnetický solenoid

*Title:*

**Optimization of laser-accelerated ion beam divergence**

*Author:* Bc. Martina Žáková

*Abstract:* The main goal of this work is theoretical study of ion acceleration during interaction of high-power ultrashort (femtosecond) laser pulses with ionized solid targets with focus on the angular spread of such generated ion beams. Crucial part is a study of ion (proton) divergence reduction, for example by various target designs or by magnetic field of a solenoid installed behind the target. According to obtained results, the beam divergence is reduced the best by the use of the target with a hole on its rear side and by the curved target. Furthermore, it is demonstrated that the magnetic solenoid is able to decrease divergence of proton beam with defined energy ten times in comparison to original value. The study is performed using two-dimensional Particle-in-cell simulations and Matlab program. This work is important for the implementation and optimization of future experiments at the ELI-Beamlines and also experiments carried out in the Institute of GIST in Gwangju, Korea.

*Key words:* proton beam divergence, laser-driven ion beams, Particle-in-cell simulations, advanced targets, magnetic solenoid

# Contents

<b>Introduction</b>	<b>1</b>
<b>1 Laser-driven ion beams</b>	<b>3</b>
1.1 Basic theoretical background . . . . .	3
1.2 Acceleration mechanisms of ion beams in solid targets . . . . .	6
1.2.1 Target Normal Sheath Acceleration (TNSA) . . . . .	7
1.2.2 Radiation pressure acceleration (RPA) . . . . .	9
1.2.3 Combined regime – TNSA-LS-RPA acceleration . . . . .	10
1.2.4 Break-Out Afterburner (BOA) . . . . .	12
1.3 Electron heating mechanisms at the critical surface . . . . .	13
1.3.1 Brunel vacuum heating . . . . .	14
1.3.2 Relativistic $\vec{j} \times \vec{B}$ heating . . . . .	14
1.3.3 Resonance absorption . . . . .	15
1.4 Divergence of laser-driven ion beams . . . . .	15
1.4.1 Decreasing divergence by advanced targets . . . . .	16
1.4.2 Decreasing divergence by beam devices . . . . .	17
1.4.3 Decreasing beam divergence in the ultra-intense short pulse regime . . . . .	21
<b>2 Applications of laser-accelerated ion beams</b>	<b>23</b>
2.1 Hadrontherapy . . . . .	23
2.1.1 Suitable energies and required properties of the beam . . . . .	25
2.1.2 Biological effects of ionizing radiation . . . . .	26
2.2 Inertial confinement fusion . . . . .	29
2.2.1 Direct drive . . . . .	29
2.2.2 Indirect drive . . . . .	30
2.2.3 Fast ignition . . . . .	31
<b>3 Particle-in-cell simulations of angular distribution of accelerated protons from advanced targets</b>	<b>34</b>
3.1 Plasma modelling . . . . .	34
3.2 Theoretical approach of Particle-in-cell (PIC) simulations . . . . .	35
3.2.1 Vlasov method versus PIC method . . . . .	36
3.3 Basic four-step Particle-in-cell scheme (PIC) . . . . .	37
3.4 Computational background . . . . .	39
3.4.1 Extendable PIC Open Collaboration (EPOCH) . . . . .	39
3.4.2 MetaCentrum . . . . .	40

3.4.3	Implementation of Energy balance . . . . .	41
3.4.4	Dimensionless energy balance . . . . .	41
3.5	Setting of input parameters and target designs . . . . .	42
3.5.1	Various targets designs . . . . .	42
3.5.2	Summary of simulation parameters . . . . .	43
3.6	Density plots of expanding targets . . . . .	44
3.7	Angular spread . . . . .	46
3.8	Energy spectrum . . . . .	48
3.9	Energy balance . . . . .	50
3.10	Phase space . . . . .	52
3.11	Fabrication of targets with microstructures and planned experiments . . . . .	54
<b>4</b>	<b>Numerical simulations of proton trajectories in magnetic solenoid</b>	<b>56</b>
4.1	Reduction of divergence by magnetic solenoid . . . . .	56
4.1.1	Applied code modifications . . . . .	57
4.1.2	Simulation parameters . . . . .	57
4.1.3	Results . . . . .	57
	<b>Summary and Conclusion</b>	<b>61</b>

# Introduction

Laser plasma physics has gathered a big interest because of its implications in numerous research fields. Very strong electric fields can be sustained in plasma, thus generating large charge displacement and, in turn, acceleration gradients in very short distances (typically in a few of micrometers). Several tens of MeV ions can be accelerated from a plasma produced by a high intensity, short laser pulse. Consequently, laser-driven ion beams have a great importance in a number of technological applications since the high intensity pulsed lasers were developed. The huge list of future utilizations includes e.g. laser triggering and control of nuclear reactions, production and probing of warm dense matter, "fast ignition" of inertial confinement fusion targets, cancer treatment etc. [1]. In contrast to electrons and X-rays, the great advantage of protons/ions used in hadrontherapy is associated with the delivery of most of their energy at the end of their path during the propagation in tissues. This characteristic, known as energy release in the Bragg peak, allows to treat the tumor cells reducing the damages in the healthy surrounding tissue [2].

Currently, the mechanisms of laser driven acceleration are being improved to obtain higher energies per nucleon up to hundreds MeV. New generation of lasers will allow to achieve much higher intensities than the present ones and will allow to accelerate ions at higher energies, thus enabling future medical applications, such as laser based hadrontherapy. The recent research is focused on improving the ion beam quality, for example by decreasing the beam divergence which is a crucial parameter for the use of such beams in multidisciplinary applications. There are many ways how to achieve more collimated beams such as applying various designs of targets [3], [4], [5] placing magnetic beam devices in the particle path [6], [7] or using ultra-intense short pulse laser regimes [8]. These approaches can be studied by means of computer simulations such as Particle-in-cell method providing valuable information before the specific experimental campaign.

In this work two numerical approaches are used to study various possibilities in decreasing angular spread of laser-accelerated ion beams. Firstly, impact of different design of targets on beam divergence is studied using two-dimensional Particle-in-cell simulations (PIC). Namely, these target types include flat foils, curved foil and foils with diverse microstructures. Secondly, another proposed method for the divergence reduction is using a magnetic solenoid. The trajectories of the laser accelerated particles passing through the solenoid are modeled in a Matlab program, where results from PIC simulations are used as input. The divergence is controlled by optimizing the magnetic field inside the solenoid (i.e. the wire current) and installing an aperture in front of the device.

From the theoretical point of view, the work is focused on the explanation of laser-driven acceleration mechanism principles, basics of relativistic acceleration scenarios (which are very promising nowadays), electron heating mechanisms (important for deeper understanding of laser acceleration) and results obtained in beam divergence-reduction field. Different applications

of laser-driven ion beams are also discussed such as inertial confinement fusion and treating of malign tumors. The hadrontherapy section follows the method description in my Bachelor's thesis [9] and enriches it with a brief look on biological effects of ionizing radiation. The theoretical background of Particle-in-cell simulations is only slightly outlined, because more advanced explanation can be found in my Research project [10].

# Chapter 1

## Laser-driven ion beams

### 1.1 Basic theoretical background

One of the main goal of this master thesis is to investigate behavior and physical principles of the generation and modification of laser driven ion beams with emphasis on the possible, both future and present, applications. The very important part of this examination is to deeply understand the physical background of accelerating mechanisms of such beams where plasma plays crucial role. Therefore, a short summary of basic plasma variables and fundamental concepts are presented bellow. For more detailed description or derivation and deeper understanding see [11], [12].

#### Definition of plasma

Plasma is a quasi-neutral system of charged or neutral particles which are coupled together by their electric and magnetic fields and show collective behavior (but it may not dominate).

#### Quasi-neutrality

Quasi-neutral system is a system whose total charge in small volume (at least one Debye length which is a distance over which quasi-neutrality may break down) is much lower than total charge of all ions. Mathematically:

$$n_e \approx Z n_i, \tag{1.1}$$

where  $n_e$  and  $n_i$  denote electron and ion density, respectively.  $Z$  is the average charge state, i.e. mean ion charge.

#### Plasma frequency

One cannot deal with quasi-neutrality of very fast phenomena, because charges can be separated for a very short moment. Thus, a simple condition for quasineutrality must be taken into account:

$$\tau \gg \omega_{pe}^{-1}, \tag{1.2}$$

where  $\tau$  is characteristic time. From equation of electron motion and differential equation of linear harmonic oscillator, one can derive the electron plasma frequency  $\omega_{pe}$  [12]:

$$v = \frac{d\Delta}{dt} \Rightarrow m_e \frac{dv}{dt} = -eE = -e \frac{\sigma}{\varepsilon_0} = -\frac{e^2 n_e \Delta}{\varepsilon_0} \Rightarrow \frac{d^2 \Delta}{dt^2} + \frac{e^2 n_e}{\varepsilon_0 m_e} \Delta = 0, \quad (1.3)$$

$$\omega_{pe} = \sqrt{\frac{e^2 n_e}{\varepsilon_0 m_e}}, \quad (1.4)$$

where  $\sigma$  is charge per unit area,  $E = \sigma/\varepsilon_0$  is the electric field in plasma,  $\varepsilon_0$  is vacuum permittivity and  $n_e$  is electron density.

Similarly, ion plasma frequency is defined as:

$$\omega_{pi} = \sqrt{\frac{n_i Z^2 e^2}{m_i \varepsilon_0}} = \sqrt{\frac{Z m_e}{m_i}} \omega_{pe}. \quad (1.5)$$

### Critical Density

Depending on whether the incident laser frequency is lower or higher than  $\omega_p$ , the plasma is so-called overdense or underdense, respectively. The density known as critical denotes the boundary between underdense and overdense plasma and is given by cut-off frequency where the light frequency is equal to the plasma frequency  $\omega_p$ :

$$\omega = \omega_p \Rightarrow \omega^2 = \frac{e^2 n_c}{\varepsilon_0 m_e}, \quad (1.6)$$

$$n_c = \frac{\varepsilon_0 m_e}{e^2} \omega^2. \quad (1.7)$$

Electromagnetic (EM) waves with frequency higher than plasma frequency  $\omega_p$  interact with underdense plasmas conductively in contrast to EM waves with frequency lower than  $\omega_p$  which assign dielectric behavior with overdense plasmas (the inertia of electrons retards their response). As a result, the underdense plasma is rather transparent to the radiation [13].

### Macroscopic parameters, Maxwell distribution function

In thermodynamic equilibrium, plasma is described by macroscopic parameters – electron and ion densities and temperatures  $n_e$ ,  $n_i$  and  $T_e$ ,  $T_i$ , respectively. The temperature can be defined for a thermodynamic equilibrium via the Maxwellian distribution function  $f(\varepsilon_{kin})$  in kinetic energy [13]:

$$f(\varepsilon_{kin}) = \frac{2}{\sqrt{\pi}(k_B T)^{3/2}} \sqrt{\varepsilon_{kin}} \exp\left(-\frac{\varepsilon_{kin}}{k_B T}\right). \quad (1.8)$$

Kinetic energy can be also expressed by equipartition theorem. Assuming that, the relation for mean thermal velocity of electrons  $v_{te}$  moving in one direction is:

$$\varepsilon_{kin} = \frac{1}{2} m_e v_{te}^2 = \frac{1}{2} k_B T_e \Rightarrow v_{te} = \sqrt{\frac{k_B T_e}{m_e}}, \quad (1.9)$$

where  $k_B$  is Boltzmann constant and  $m_e$  means electron mass.

## Collision frequency

The thermal equilibrium is ensured by collisions. The rate of the momentum transfer between particles is expressed by collision frequencies. We distinguish collisions according to their collision angle into scattering at large angles (bigger than  $90^\circ$ ) or at small angles which are more frequent in plasma. For both cases, the collision frequency could be derived with the assumption that electron velocity is bigger than thermal velocity  $v_0 \gg v_{Te}$  [12]:

$$\nu_{c \text{ large}} = \frac{4\pi n_0}{(4\pi\epsilon_0)^2} \frac{q^2 q_0^2}{m^2 v_0^3}, \quad (1.10)$$

$$\nu_{c \text{ small}} = \frac{8\pi n_0 e^4}{(4\pi\epsilon_0)^2 m_e^2 v_0^3} \ln\Lambda, \quad (1.11)$$

where  $v_0$  is electron speed,  $\ln\Lambda$  is Coulomb logarithm and  $n_0$  is particle density. These relations are the most frequent ones, but in fact, collision frequency can be derived for each action by statistical approach from Fokker-Planck (FP) equation (the solution process is demonstrated in [11]). Collision frequency does not rely on velocity when it is slow, e.g. flow of electric current. On the contrary, for rapid particles the collision frequency  $\nu_c$  decreases rapidly with increasing velocity and scales as:

$$\nu_c \sim v_0^{-3}, \quad (1.12)$$

which is actually the case of collisional frequencies (1.10) and (1.11). Thus, for high speed particles we can work under approximation of collisionless plasma.

## Debye length

Charged plasma particles are influenced by the generated electric field which can be decomposed into two components – average field and fluctuations over the Debye length  $\lambda_D$ , i.e.  $\vec{E}_{micro} = \langle \vec{E} \rangle + \delta\vec{E}$ . Debye length is the length over which the field contribution of a single charge is shielded by the surrounding electrons [13].

Charges can be spontaneously separated only at a distance allowed by their thermal energy, i.e. the distance, where all the heat energy changes into potential one. Taking  $\Delta$  as a thickness of electrons layer moving from ion background, the potential energy of electron is equal to its thermal energy, when it moves over one  $\Delta$  [12]:

$$U_{pot} = -eE\Delta = \frac{e^2 n_e \Delta^2}{\epsilon_0} = k_B T_e. \quad (1.13)$$

Then, the electron Debye length is given by:

$$\lambda_{De} \equiv \Delta = \sqrt{\frac{\epsilon_0 k_B T_e}{n_e e^2}}. \quad (1.14)$$

The number of particles within the so-called Debye sphere is called plasmatic parameter  $N_D$  and is given by:

$$N_D = \frac{4\pi}{3} \lambda_{De}^3 n_e. \quad (1.15)$$

When  $N_D \gg 1$ , we are talking about *ideal plasma*.

## Collective behavior

The term collective behavior denotes particle interaction by macroscopic electromagnetic fields unlike microscopic ones by which the particles interact with binary collision. A collective action is characterized by the electron plasma frequency  $\omega_{pe}$  which is stronger than the binary operation characterized by collision frequency  $\nu_c$ , i. e.  $\omega_{pe} > \nu_c$  [12].

## 1.2 Acceleration mechanisms of ion beams in solid targets

Apart from conventional acceleration techniques there is also a possibility to produce particle beams by ion acceleration based on high intensity laser interaction with matter. These beams are comparable with those from conventional accelerators in terms of brightness, pulse duration, emittance and compact source size. Due to their parameters (e.g. energy, divergence, ...) they can be used for various applications including fast ignition, proton radiography, development of compact facilities for laser-driven ion beam radiotherapy, hadrontherapy (a healing of radiation-resistant tumors), nuclear research and many others [7].

The main problem laser accelerators have to face is the typical high divergence of the accelerated beams together with the high energy spread, which does not fulfill the requirements for therapy or other applications. Thus, the main effort is focused in reducing the beam divergence.

There are two main acceleration scenarios able to explain the observation of fast ions in a typical experiment on femtosecond laser pulse interaction with solid foil targets. Both of them are schematically shown in Fig. 1.1. In the first scenario called Radiation Pressure Acceleration (RPA), the electrons are pushed into the target by ponderomotive force (i.e., by the radiation pressure of the incident laser beam) and the ions are accelerated from the target front side by the generated electrostatic field. The force is so strong that it can push an overdense target inwards, which causes a sharp growth in density profile and changes the shape of its surface. This phenomena is known as Hole boring. RPA could be more efficient with circularly polarized laser pulses [14], [15]. The second scenario which is based on a generation of hot electrons is called Target Normal Sheath Acceleration (TNSA) and is very common in experiments. In a nutshell, laser pulse generates a population of very energetic hot electrons which can pass through the target and cause unbalance in charge on the target rear side. The resulting electrostatic field finally leads to the acceleration of ions.

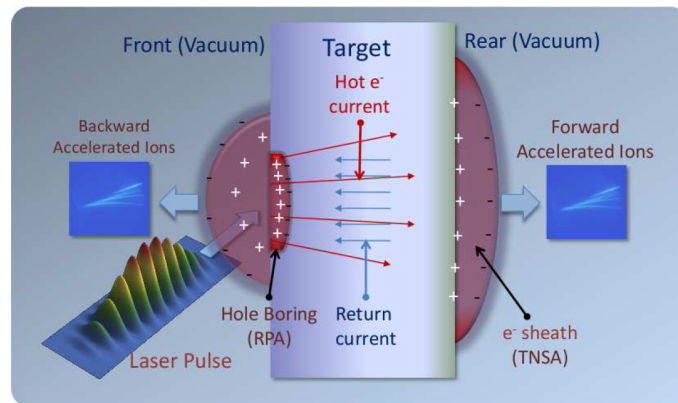


Figure 1.1: A simple sketch of laser-driven ion acceleration from thin foils; [1]

Planar thin metallic or plastic foil targets are usually used in experiments due to their easy characterization and positioning. Ions accelerated in such targets are mainly protons originated from low-Z hydrocarbon or water deposits [16], [17]. In experiments, 100-MeV class protons accelerated from the interaction of a short laser pulse with a thin target have been demonstrated [18].

### 1.2.1 Target Normal Sheath Acceleration (TNSA)

The proton acceleration by an ultraintense laser pulse ( $> 10^{19}$  W/cm<sup>2</sup>) was explained by the Target Normal Sheath Acceleration (TNSA) model [19]. The scenario is demonstrated in Fig. 1.2. Firstly, a very intense current of hot electrons can be generated on the front side of the target. When the hot electrons reach its rear side, they cause an unbalance in charge resulting in a strong electrostatic potential. For better understanding, we can imagine that as a double layer of positive (ions) and negative (electrons) charges, which generates an electrostatic field. As soon as electrons reach the rear side and pass the target-vacuum boundary they can be attracted back to the target. In fact, the most energetic ones escape, but the majority of electrons return back to the target (because of acceleration by electrostatic force) or even reach the front side where the TNSA mechanism can be observed as well or they start the cycle again. Due to the electrostatic field, the ions on the target rear side will be ionized and accelerated. The direction of the accelerated ions from the rear side is typically normal to the target (forward acceleration following the direction of the electric field), therefore the mechanism is commonly known as Target Normal Sheath Acceleration (TNSA). The accelerated ions leave the target together with co-moving electrons forming a quasineutral plasma cloud. Because the plasma density in this volume drops dramatically after the detachment from the target and temperature stays high, recombination effects are negligible for propagation lengths in the range of several meters [20].

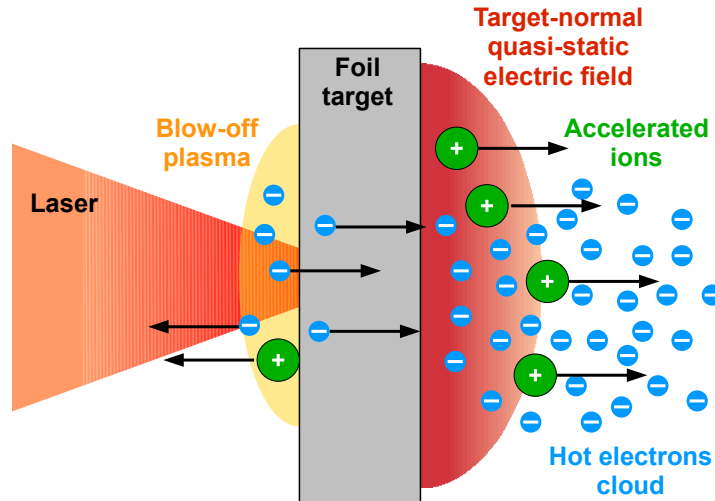


Figure 1.2: Target normal sheath acceleration

In fact, the species of accelerated ions depends on the purity of the target. If the target contains a water or hydrocarbon contaminants on its surface, protons are accelerated the most because to their highest charge-to-mass ratio. Thus, for efficient acceleration of heavy ions one must have a very pure target which we can obtain by various techniques like target heating or laser ablation [21].

TNSA can be mathematically described by the model of free isothermal expansion into a vacuum of a plasma occupying initially a space in front of the target ( $x < 0$ ). From Poisson equation (1.16), equation of motion (1.17) and continuity equation (1.18) we will get the self-similar solution in the form of rarefaction wave (1.19). This solution is valid on the scale length larger than the Debye radius, where assumption of quasineutrality is valid.

$$\Delta\phi = \frac{\rho}{\epsilon_0} = \frac{e}{\epsilon_0} (n_e - Zn_i), \quad (1.16)$$

where  $\phi$  is electric potential,  $e$  is elementary charge,  $\epsilon_0$  permittivity,  $Z$  is atomic number,  $n_e$  is the electron density satisfying the Boltzmann distribution  $n_e = n_{e0} \cdot \exp(e\phi/T_e)$  and  $n_i$  is the ion density defined as  $n_i = 0$  for  $x < 0$  or  $n_i = n_{i0}$  for  $x > 0$  at the beginning of expansion.

$$\left( \frac{\partial}{\partial t} + v_i \frac{\partial}{\partial x} \right) n_i = -n_i \frac{\partial v_i}{\partial x}, \quad (1.17)$$

$$\left( \frac{\partial}{\partial t} + v_i \frac{\partial}{\partial x} \right) v_i = -\frac{Ze}{m_i} \frac{\partial \phi}{\partial x}. \quad (1.18)$$

Now, self-similar variable is defined as  $\xi = x/t$  and the quasineutrality condition  $n_e = Zn_i$  is taken into account. Then, the solution of set of equation (1.16) - (1.18) describes rarefaction wave:

$$Zn_i = n_{e0} \cdot \exp(-\xi/c_s - 1), \quad v_i = c_s + \xi, \quad e\phi = -T_e (\xi/c_s + 1). \quad (1.19)$$

The relation for maximum accelerating electric field is obtained by integrating (1.16) from  $x = 0$  to  $x = \infty$ , [13]:

$$E_{ac} \approx \frac{T_e}{e\lambda_{D0}} = \sqrt{\frac{n_{e0}T_e}{\epsilon_0}}, \quad (1.20)$$

the variable  $T_e$  denotes the product  $T_e \equiv T_{el}k_B$ , where  $T_{el}$  is the electron temperature and  $k_B$  is Boltzmann constant,  $\lambda_{D0}$  is Debye length in the unperturbed plasma of electron density  $n_{e0}$ .

The dependence of electron temperature  $T_{el}$  on ponderomotive potential of the laser  $U_p$  is following [22]:

$$T_{el} = m_e c^2 \sqrt{1 + 2 \frac{U_p}{m_e c^2}}, \quad (1.21)$$

and  $U_p[\text{eV}] = 9.33 \times 10^{-14} I[\text{W}/\text{cm}^2] \lambda^2[\mu\text{m}]$ .

Because the system acts as a rarefaction wave, its front is moving with the maximum ion velocity. This maximum speed can be transferred into the cutoff energy of accelerated ions:

$$\varepsilon_{imax} \approx 2ZT_e \ln^2 \left( \tau + \sqrt{\tau^2 + 1} \right), \quad (1.22)$$

and subsequently into total energy of accelerated ions [13]:

$$W_{itot} = \int \varepsilon_i \frac{dN}{d\varepsilon_i} d\varepsilon_i = ZT_e n_{i0} c_s t_{acc}, \quad (1.23)$$

where  $t_{acc}$  is ion acceleration time. Moreover, the laser-to-ion conversion efficiency can be expressed as the ratio of  $W_{itot}$  and the laser pulse energy  $\varepsilon_{Ltot}$ :

$$\eta_i = W_{itot}/\varepsilon_{Ltot}. \quad (1.24)$$

In TNSA regime, the maximum ion/proton energy is determined by the hot electrons (see relation (1.23)) and consequently, the maximum proton energy is dependent on the peak intensity of laser pulse with scaling  $\sim I^{\frac{1}{2}}$  [1].

## 1.2.2 Radiation pressure acceleration (RPA)

There is also a possibility of developing a significant contribution to ion acceleration at the front surface of the target, where the mechanisms act on ions at the front side in the vicinity of the laser focus. The main idea is that the intense radiation pressure of the laser pulse, represented by ponderomotive force, pushes an overdense target inwards, which causes a sharp growth in density profile and changes the shape of its surface. This process is known as "hole boring". In other words, when the laser pulse reaches the critical surface it forces the target electrons inwards and electrostatic field is growing as a result of charge separation balancing the ponderomotive force. In fact, this can be expressed by balance between total radiation and electrostatic pressure as follows:

$$\frac{1}{2}\varepsilon_0 E_{es}^2 = \frac{1+R}{c} I_L \approx \frac{2}{c} I_L, \quad (1.25)$$

where  $E_{es}$  is electric field caused by charge separation,  $I_L$  is laser pulse intensity,  $R$  is target reflectivity (usually taken as  $R \approx 1$ ),  $\varepsilon_0$  is vacuum permeability and  $c$  is speed of light.

When the electrons are pushed into the target, the ions due to the charge separation on the front side are free to be accelerated by electrostatic field  $E_{es}$  and their maximum energy is:

$$\varepsilon_{imax} = \frac{Zm_e c^2 a^2}{m_i \gamma_L}, \quad (1.26)$$

where  $Z$  is atomic number,  $m_e$  is mass of electron,  $m_i$  is mass of ion,  $c$  is speed of light,  $a$  is dimensionless laser amplitude expressed as  $a = eE_0/m_e c \omega$  and  $\gamma_L$  is relativistic gamma factor of the laser  $\gamma_L \approx \sqrt{1+a^2}$  [13].

In contrast with TNSA we get linear scaling of maximum ion energy with laser intensity  $I$  instead of  $I^{\frac{1}{2}}$ , which is clearly a great advantage. On the other hand, the front surface acceleration is expected to produce a large-divergent ion beams due to the curved critical density interface where the charge separation is present (hole boring). The "hole boring" acceleration is considered as a particular regime of the radiation pressure acceleration (RPA). Another aspect which have to be taken into account is polarization of the laser pulse. If the laser pulse is linearly polarized, many experiments demonstrate that TNSA produces higher energy particles with smaller divergence and a higher efficiency than RPA [13]. Nevertheless, radiation pressure acceleration mechanism prevails with circularly polarized laser beams at normal

incidence on a foil, which can suppress most electron heating mechanisms such as resonance absorption, vacuum heating,  $\vec{j} \times \vec{B}$  heating etc.

RPA regime is normally suitable for ion acceleration by a laser pulse with peak intensity  $\gtrsim 10^{23}$  W/cm<sup>2</sup>. However this intensity can be lowered to  $\sim 10^{21}$  W/cm<sup>2</sup> by focusing a circularly polarized laser pulse on a nanometer-thick target. RPA-dominated regime is suggested for quasimonoenergetic proton/ion generation.

### 1.2.3 Combined regime – TNSA-LS-RPA acceleration

#### Quick summary of two basic acceleration mechanisms

Usually two main scenarios in laser acceleration of particle beams are taken into account: TNSA and RPA. In addition, recent studies proved that this scenarios can work, blend together and create a new accelerating mechanism called hybrid Target normal sheath acceleration – Light sail (TNSA-LS) acceleration [23].

As we have already discussed in detail in chapter 1.2.1, in TNSA mechanism the acceleration of ions is ensured by the strong electrostatic sheath field at the rear side of the target. This field is created by the population of hot electrons generated at the front (laser-irradiated) side of the target. As a consequence, electrons travel through the target at a speed close to  $c$ .

RPA mechanism described in subsection 1.2.2 can be realized with two different geometries – Hole Boring (HB) and Light Sail (LS). In HB regime, electrons are pushed inwards by the non-oscillating ponderomotive term and accrue in a compressed layer, which includes a charge separation electric field  $E_z$  accelerating ions. Thus, HB can also causes a change in the shape of the target surface. In LS regime [24], the target is assumed to be a perfect plane mirror (i.e. rigid and totally reflecting) boosted by a light wave at perpendicular incidence. The presumption of perfect mirror implies that all the ions are accelerated to the same velocity, thus, the spectrum is monoenergetic. The great advantage of LS regime is that it predicts the ion energy and corresponding conversion efficiency  $\eta$  (i.e. the fraction the laser pulse energy transferred into quasi-monoenergetic ions), although according to simulation results [24], the evaluation of  $\eta$  is overestimated. In contrast with TNSA, RPA accelerates beams with quasimonoenergetic spectrum, requires higher intensities and uses mainly circular polarized laser pulses (TNSA linear polarized pulses), which can provide a constant ponderomotive drive. The basic principle is to use the ultrastrong radiation pressure to accelerated protons to relativistic energies during a few laser cycles. This phenomena takes a few time, thus, this stage is done before the rapid growth of the rear sheath field and the heavy decompression of the foil. As a result, the protons can catch up with the electrons [23].

#### A hybrid TNSA-LS regime itself

If the target has favorable dimensions (it is thick less than half of the pulse length, but thick enough to prevent the laser from punching through), the electrons recirculate through the target and thus, the hot electron density increases. This leads to the electrostatic sheath field required for TNSA but also to rapid foil deformation, breaking the equilibrium condition required for LS RPA. To achieve the RPA dominance with linear polarized laser pulse (more suitable for TNSA regime), the target must be very thin to allow Hole boring reach the foil rear surface early enough within the laser pulse duration [23]. When the condition (1.27) is satisfied, the ions from the front side accelerated by HB RPA join those accelerated via TNSA

at the rear side and experience a *hybrid TNSA-LS acceleration*.

$$l_0 < v_b \tau_L, \quad (1.27)$$

where  $l_0$  is thickness of the target,  $v_b$  is HB velocity and  $\tau_L$  is laser pulse duration. Moreover, the coupling condition of the RPA dominance can be derived [23], where the left part describes the requirement to avoid complete electron blow-out from the foil target:

$$\frac{1}{\pi} \frac{n_c}{n_0} a < \frac{l_0}{\lambda} < \frac{1}{2\pi} \sqrt{\frac{n_c}{\gamma n_0}} a \exp \left[ \sqrt{\frac{Z n_c}{n_0}} \frac{a}{\sqrt{\gamma - 1}} \left( \frac{n_0}{\gamma n_c} \right)^{1/4} + \frac{1 - \ln 2}{2} \right], \quad (1.28)$$

where  $n_0$  is the initial foil electron density,  $n_h = n_c \gamma$  is assumed to be the effective hot-electron density,  $\gamma = (1 + a^2)^{1/2}$  and  $a$  is dimensionless laser amplitude  $a = e|E_L|/(m\omega c)$ , where  $|E_L|$  is the amplitude of the laser field oscillating at frequency  $\omega$ ,  $\lambda$  is laser wavelength,  $A$  and  $Z$  are the ion mass and charge number satisfying  $n_0 = Z n_i$  and  $m_i = A m_p$ .

The ions are accelerated by various mechanisms demonstrated in Fig. 1.3 depending on validity of the condition (1.28). There are three lines of possible hybrid acceleration started with HB stage and ending by LS RPA. When the condition (1.28) is fulfilled the blue line is taken and high-energy quasimonoenergetic ion beams can be obtained. If the foil is thicker than required by relation (1.28), but thin enough to satisfy equation (1.27), ion acceleration takes place in a hybrid stage where RPA and TNSA compete (black and purple lines). In these lines TNSA contribute only as a small leakage. Finally, if the target is thick, thus it does not satisfy both condition (1.27) and (1.28), ions undergo a pure TNSA acceleration (purple line) or TNSA dominated acceleration (green line).

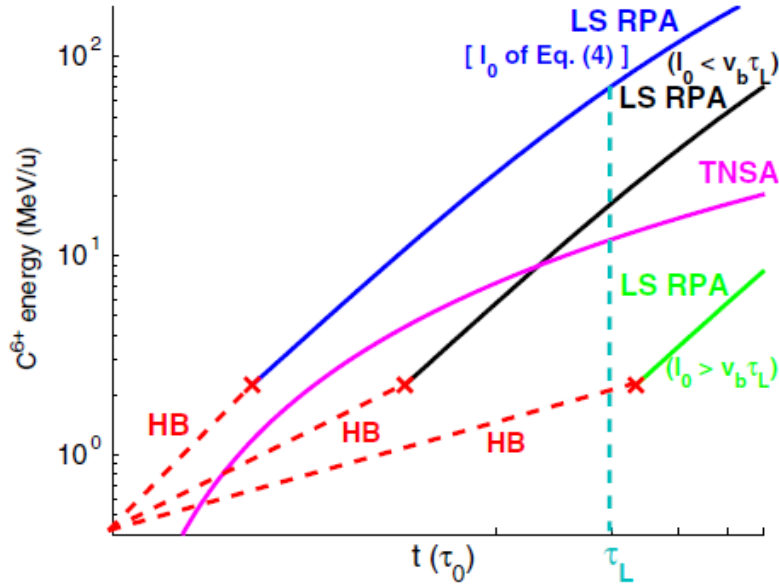


Figure 1.3: Three regimes for ion acceleration from thin foils by linearly polarized laser pulses, based on (1.27), (1.28): RPA-dominated (blue lines), competing of RPA and TNSA (black and purple), and TNSA-dominated (purple and green), where the cross point corresponds to the transition time from HB-RPA to LS-RPA; [23]

In the combined hybrid regime, beam divergence  $< 5^\circ$  and energy spread  $\sim 0.1$  GeV of 1.26 GeV quasimonoenergetic  $C^{6+}$  ion beam were demonstrated in two-dimensional particle-in-cell simulations of 80 nm ultrathin foils irradiated by linearly polarized pulses at intensities  $10^{21}$  W/cm<sup>2</sup> [23].

### 1.2.4 Break-Out Afterburner (BOA)

A new laser acceleration regime based on relativistic transparency of a target is known as Break-Out Afterburner (BOA) acceleration [25], [26], [27], [28].

BOA mechanism usually plays a crucial role when an ultrahigh intensity laser pulse interacts with an ultrathin target of density about  $\sim 10^{23}$  cm<sup>-3</sup>. Electrons are heated to high temperature by the laser which drives a hydrodynamic longitudinal expansion of the target along the laser propagation axis. These energetic electrons are called "hot" and they are produced in the laser field at the target front side. With becoming more and more electrons "hot", the electron density decreases and the electron Lorentz factor  $\gamma_e = \sqrt{1 - (v_e/c)^2}$  increases. Thus, the laser field can go deeper to the still opaque target and further enlarges the hot electron generation. For a thin target ( $\sim nm - \mu m$ ) the laser field can convert all the electrons into hot generation and the target become relativistically transparent (mathematically, the condition  $n_e/n_{crit}\gamma \approx 1$  is satisfied). It is proved that when the target becomes relativistically transparent to the laser (time  $t_1$ ), an epoch of dramatic acceleration of ions (BOA) occurs and lasts until the electron density in the expanding target reduces to the critical density in the non-relativistic limit (time  $t_2$ , the condition  $n_e/n_{crit} < 1$  is satisfied), see Fig. 1.4 [27].

An electrostatic field is created by the laser pulse propagating through the target and pushing the electrons forward. The electrons transfer energy to the ions by this field and then, is replenished by the laser immediately.

Recent experiments claimed to work in the BOA regime and the accelerated carbon ion peak energy was the highest demonstrated to date [27].

In contrast to RPA, which requires very high laser intensities ( $> 10^{22}$  Wcm<sup>-2</sup>) and short pulses ( $< 100$  fs), BOA acts with lower intensities ( $\sim 10^{20}$  Wcm<sup>-2</sup>) and longer laser pulses ( $\sim 500$  fs) which make this mechanism more accessible for current laser systems [27].

Comparing the BOA and RPA with TNSA mechanisms, there are four main differences [27]:

- The laser interacts directly with electrons co-propagating with the beam ions in BOA and RPA, in contrast to TNSA scenario
- Accelerating fields of BOA and RPA are bigger than those of TNSA, thus, we can expect higher energies of accelerated ions
- In RPA and BOA the high-Z species see comparable accelerating fields as protons, whereas in TNSA the protons shield the fields from the heavier species, thus, heavier ions are accelerated to higher energies compared with TNSA
- Different dynamics of laser target interaction during BOA leads to a fundamentally different angular distributions of the ions compared with TNSA [29]; fastest ions are emitted off-axis in a plane orthogonal to the laser polarization

It is shown that when the target becomes relativistically transparent to the laser (time  $t_1$ ), an epoch of dramatic acceleration of ions (BOA) occurs that lasts until the electron density

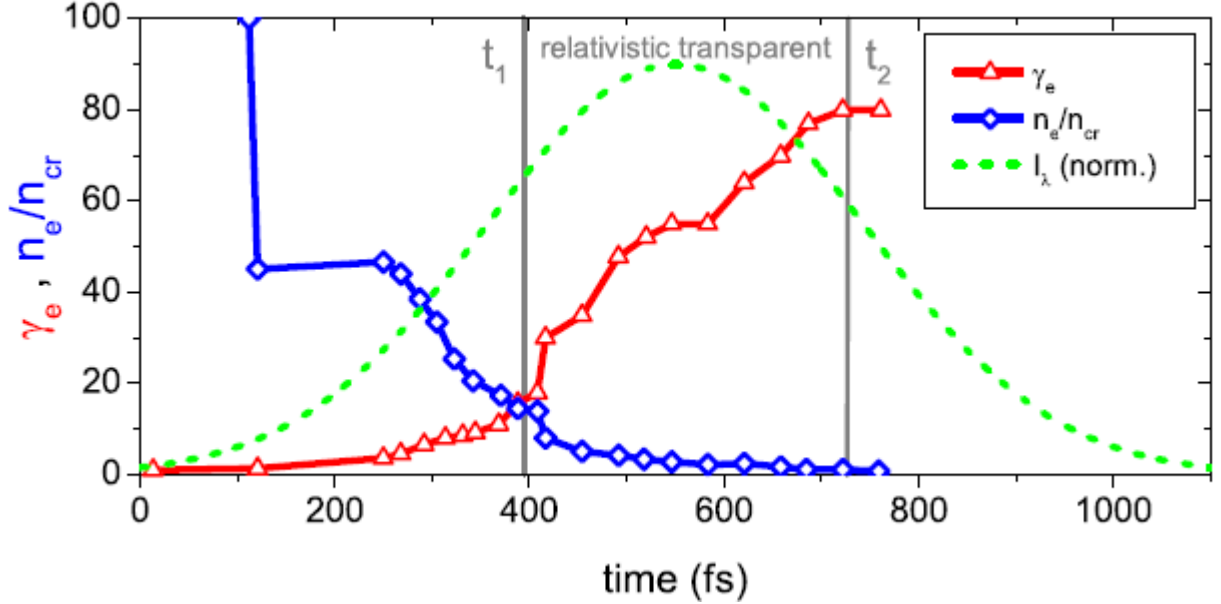


Figure 1.4: Target expansion and laser-plasma interaction during BOA: the picture shows the electron Lorentz factor  $\gamma_e$  (red), electron density  $n_e/n_{crit}$  (blue) and normalized laser amplitude (green) as a function of time. After  $t_1$  the plasma is classically overdense, yet relativistically transparent with  $n_e/n_{crit} < 1$ . After  $t_2$  the plasma turns classically underdense with  $n_e/n_{crit} < 1$ ; [28]

in the expanding target reduces to the critical density in the non-relativistic limit (time  $t_2$ ), see Fig. 1.4 [27].

### 1.3 Electron heating mechanisms at the critical surface

Target normal sheath acceleration is the most experimentally observed ion acceleration mechanism and hot electrons play a crucial role in it. Thus, studying electron heating mechanisms is very important.

The heating mechanisms can be divided into two groups depending on the laser intensity:

- If the laser intensity is below  $10^{15}$  W/cm<sup>2</sup>, the plasma is heated by *electron-ion collisions* and absorption mechanisms such as collisional absorption, normal and anomalous skin effect cause heating of all electrons. Relatively long time is needed for efficient heating, which corresponds to longer ( $\sim ns$ ) pulses usually employed in such interactions. Then, more than 80% of the laser pulse energy can be delivered into plasma.
- If the laser intensity is higher than  $10^{16}$  W/cm<sup>2</sup>, the plasma is heated predominantly by *collisionless absorption mechanisms*. If the plasma has step-like or very steep density profile, the absorption of laser energy takes place due to Brunel vacuum heating or  $\vec{j} \times \vec{B}$  heating. On the other hand, if the plasma density profile has the scale length larger than the laser wavelength, the resonant absorption plays a crucial role. In contrast to collisional heating mechanisms, in collisionless ones only a part of electrons gain most of absorbed energy; such population of fast electrons is called *hot*.

## Hot electrons

The relaxation time of hot electrons is large compared to the plasma expansion time. Thus, after interaction two temperatures  $T_h, T_c$  (hot and cold electrons) are considered with Boltzmann distribution for electron density:

$$n_e = n_h + n_c = n_{h0}\exp(e\varphi/T_h) + n_{c0}\exp(e\varphi/T_c), \quad (1.29)$$

where  $\varphi$  is the electrostatic potential and  $T_h$  can be found experimentally or can be estimated from ponderomotive potential  $U_p$  [22], [13], see equation (1.21) where  $T_{el} \equiv T_h$ .

### 1.3.1 Brunel vacuum heating

In this scenario, the p-polarized laser pulse (polarized light with its electric field along the plane of incidence) is obliquely incident on the surface, thus, the electric field can pull electrons out of the steep plasma. This mechanism works for high laser intensities, because amplitude of oscillating electrons driven by electric laser field is larger than the density scale length, so electrons will bring away and transform the energy of laser pulse to the kinetic energy of the plasma when they reach the overdense plasma region [30], [13].

Assuming that the overdense region is located at  $z < 0$ , the electric field of obliquely incident laser wave has two components – oscillating perpendicular or parallel to the surface. Then, electric field is given by:

$$E_z(t) = E_p \sin(\omega t + \phi) = E_0 \sin(\alpha) \sin(\omega t + \phi), \quad (1.30)$$

where  $E_p$  is the oscillating electric field perpendicular to the plasma surface,  $E_0$  is electric field amplitude and  $\alpha$  is the incidence angle of the wave.

The energy deposited by Brunel vacuum heating is transported by hot electrons in the bunches ejected once per laser period. Firstly, the electrons are pushed inside the plasma, where they obtain only a small amount of energy because of the electric field which is strongly attenuated in plasma (case  $(\omega t + \phi) \in (0; \pi)$  and  $E_z > 0$ ). Contrarily, electrons gain very high energy in the second half laser period when they are ejected into vacuum (case  $(\omega t + \phi) \in (\pi; 2\pi)$  and  $E_z < 0$ ). Time of electron expulsion influences electron trajectory. Moreover, the self-consistent electric field is created, when many electrons are ejected simultaneously. As a consequence of oscillating laser field and self-consistent electric field, the most electrons turn back into the plasma without restoring forces behind the skin layer.

The average energy of electrons is proportional to ponderomotive potential  $\varepsilon_e \sim U_p$ , where  $U_p = m_e c^2 \left( \sqrt{1 + a_p^2} - 1 \right)$ ;  $a_p$  is dimensionless amplitude of the field oscillating perpendicularly to the surface given by  $a_p = a \sin \alpha$  where  $a$  is dimensionless laser amplitude defined earlier and  $\alpha$  is the incidence angle of the wave. In most cases, the distribution of such electrons is considered to be maxwellian because the electrons are accelerated in different phases of the laser field [13].

### 1.3.2 Relativistic $\vec{j} \times \vec{B}$ heating

Contrary to Brunel vacuum heating,  $\vec{j} \times \vec{B}$  heating is the electron heating scenario also for the normal incidence of laser pulse onto the target, when the oscillating part of the electric

field perpendicular to the plasma surface  $E_p$  is zero. This scheme becomes important for relativistic laser pulse intensities i.e. when  $a > 1$  (where  $a$  is given by  $I\lambda^2 = 1.38 \cdot 10^{18} \cdot a^2$ ). In this case, the  $\vec{v} \times \vec{B}$  component of the Lorentz force can heat electrons.

Another difference between Brunel and  $\vec{j} \times \vec{B}$  heating is that in  $\vec{j} \times \vec{B}$  scenario bunches of hot electrons are ejected twice per laser period. In fact, this is the point how distinguish between Brunel and  $\vec{j} \times \vec{B}$  heating in numerical simulations.

The force which ejects electrons twice per laser period in the normal direction, acts as follows [13]:

$$F_p \sim \frac{m_e \omega c a^2}{\sqrt{1 + a^2}}. \quad (1.31)$$

Ejected electrons create self-consistent field which, together with the oscillating force of the order of  $F_p$ , returns electrons back into the plasma, similarly to Brunel vacuum heating. Moreover, same as in Brunel model, those electrons feel no restoring forces after passing skin layer. Similarly to Brunel heating, the average energy of electrons is  $\varepsilon_p \simeq U_p$ , when  $U_p$  is characteristic electron energy given by  $U_p = m_e c^2 (\sqrt{1 + a^2} - 1)$ .

### 1.3.3 Resonance absorption

Quasi-monochromatic pencil beam of laser-driven protons generated using a conical cavity target holder When a p-polarized laser pulse is obliquely incident on a continuously increasing plasma density profile, then resonant absorption will dominate as a collisionless absorption mechanism.

Firstly, the laser wave with incidence angle  $\alpha$  gets through the underdense plasma. Naturally, laser wave reach the critical surface, where the electron density can be expressed as  $n_e = n_{crit} \cos^2 \alpha$ , and will be reflected there. Electron plasma wave is resonantly excited by laser field at critical density surface. Subsequently, this wave is damped by various mechanisms – for lower intensities by collisions and Landau damping, for higher intensities by particle trapping and wave breaking [13].

## 1.4 Divergence of laser-driven ion beams

The ion beams produced from flat target are typically divergent with half angle  $0^\circ - 25^\circ$ , depending on proton energy, since the expanding field front on the target rear side is Gaussian in shape [4], [31].

Improvements in the quality of the laser-driven proton beams produced from flat foil target, thus, decreasing their divergence, have been demonstrated by small devices installed close to the target [6], [9] or by using various targets. For instance *double layer targets* [32] can produce collimated and monoenergetic proton beams, *curved* [33] or *(micro)structured targets* [5] focuses a divergent beam, where focal length is determined by the target curvature. Monochromatic collimated laser-driven proton beam can be obtained by using *microlense devices with two synchronized carefully aligned high-intensity laser beams* [34]. Moreover, the *assembled target — flat-target* [3] and *microlense attached* [35] are making the proton beam divergence smaller without any additional laser beam. In addition, a *conical cavity target holder* has been used to produce quasi-monochromatic pencil beam [7]. Some of these methods will be discussed in the next sub-chapters.

### 1.4.1 Decreasing divergence by advanced targets

#### Decreasing divergence by ultra-thin targets

In comparison to  $\mu\text{m}$  targets, more than 10 times reduction in the divergence, when using the nanometer thick foils, was demonstrated. Proton beams obtained in recent experiment had extremely small divergence about half angle only  $2^\circ$ . These beams demonstrate surprising collimation over the whole energy range and reach 6 MeV [3]. Similar results were obtained from 2D particle-in-cell simulations with parameters representing the experiments which also establish that the small divergence  $\theta$  is a result of a steep longitudinal electron density gradient and it does not noticeably depend on energy [3]:

$$\theta = \arctan \left\langle \frac{\partial n_e}{\partial y} / \frac{\partial n_e}{\partial z} \right\rangle, \quad (1.32)$$

where the angle brackets denote the average along the trajectory and  $y$  and  $z$  are the transversal and the longitudinal dimension, respectively. The laser pulse propagates along  $z$ -axis with target normal incidence. In addition, 2D simulations show interesting scaling laws. The first for divergence and the laser FWHM diameter  $\theta \sim (D_L)^{-1/2}$  and the second for divergence and laser intensity with other parameters unchanged  $\theta \sim (I_0)^{1/4}$  [3].

In general, experimental results, mainly based on TNSA mechanism, show that reduction in foil thickness implies beams with smaller divergence [3]. In addition, beam divergence depends on the electron density and electron phase space distribution behind the target. These parameters are influenced by the laser profile and then changed during the path through the target [3].

#### Decreasing divergence by curved targets

There is another way how to compensate divergence. Curved back surface of the target causes that the accelerated proton beam will converge. In Ref. [4] ion beam focusing dynamics is studied with picosecond and micrometer time/space resolution. Curved targets are irradiated by a high intensity short pulse laser. Moreover the experiments are coupled with 2D PIC simulations and the main results are [4]:

- $\sim 30 \mu\text{m}$  convergence diameter is observed for ion beam accelerated from  $800 \mu\text{m}$  diameter curved target
- significant filamentation occurs in the converging plasma
- focus location depends on proton energy; most of protons focus at the geometric target center
- the exact location of laser illumination on the curved target modifies the directionality of the ion beam, but it does not affect the ability to focus

#### Decreasing divergence by targets with micro-structures on their rear side

Using microstructures on the target rear side was considered to be a way how to decrease divergence and, thus, improve the quality of ion beams for applications. Two cases of the laser

impact on the rear surface of the target are depicted in Fig. 1.5. Naturally, when the laser focus is located between the walls, the walls create a shielding electric field which finally leads to much lower divergence typically about  $\sim 2^\circ$  (case rear1). In contrary, when the laser focus is located opposite of the wall (thus, lying in a line, corresponding to the case rear2) shielding of the normal direction is formed and protons cannot be accelerated in this direction. This leads to large divergences with half angles about  $\sim 10^\circ$ . The interpretation of previous two cases gives an important rule: a proton angular distribution is strongly dependent on the relative position of the laser focus and the microstructure on the rear surface. Thus, for larger focal diameter than the microstructure period, the relative position of the laser focus do not affect the angular divergence [5].

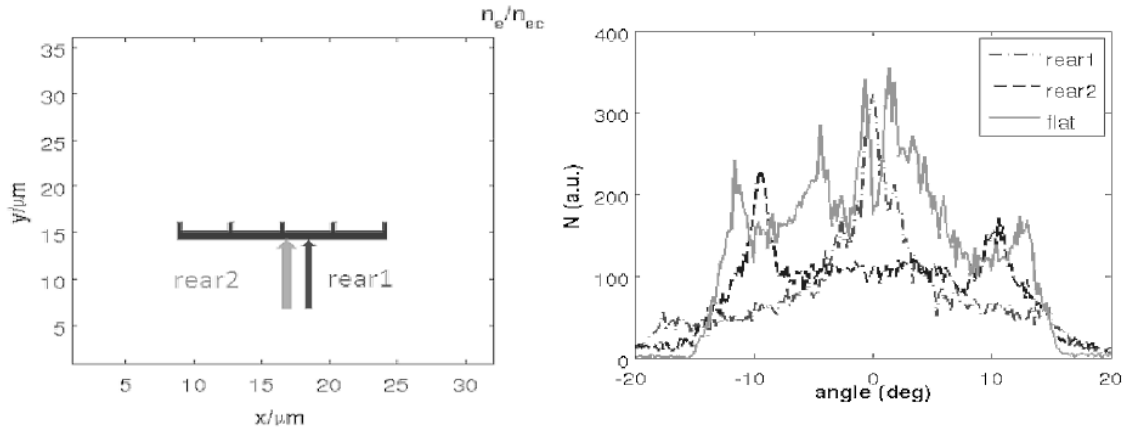


Figure 1.5: (a) Schematic of the foil target with the structure at the rear side (arrows denote focus center position in 2 different simulations); (b) angular distribution of protons accelerated to energy  $> 30$  MeV; [5]

## 1.4.2 Decreasing divergence by beam devices

### Magnetic Solenoids

Laser-driven proton beams are broadband and they have large divergences. In fact, high yields (up to  $10^{13}$  protons per laser pulse) and ultra low emittances (transversely 100-fold better and longitudinally at least  $10^4$ -fold better than conventional accelerators) are typical for such beams [36], [37]. Possible applications of magnetic solenoids include e.g. hybrid system that combines a laser accelerated source with conventional post-accelerator [37] or beam transport for hadrontherapy [36] but both applications will require efficient capture and collimation by focusing elements, e.g. magnetic lens. So far the capture of protons and electrons were demonstrated also by permanent quadrupole magnets (PMQs) where magnetic lenses were coupled with laser accelerators. The crucial disadvantage of PMQs is that their magnetic field on the order of 1 T cannot sufficiently capture highly divergent protons of more than a few MeV (and proton therapy requires protons of energies 150 – 250 MeV).

A picosecond time scale is used for laser acceleration of protons, thus, a pulse power solenoid was used to generate temporally short but intense magnetic fields. For possible proton therapy application, it is crucial to understand how many protons emerge from the solenoid and how to reduce their divergence. In addition, solenoids are used also as energy selectors [36]. Never-

theless, a typical requirement for proton therapy is a 2 – 4 Gy dose to a 1 liter volume tumor in a few minutes or less [38].

Improvements in the quality of the laser-driven proton beams produced from flat-foil target, thus, decreasing their large divergence, have been demonstrated by small beam optic devices installed close to the target. For instance, magnetic solenoid can be used in transport system of the beamline. The crucial for understanding this focusing phenomena is to understand the beam dynamics in solenoid magnetic field. A detailed description can be found in Ref. [9].

*Focusing of charged beams in a solenoid magnetic field can be described by a simple geometry:* We will assume the charged particle beam, where only four particles on the beam surface ( $A, B, C, D$ ) will be taken into account for studying beam behavior. Each particle moves on a circular trajectory in the  $x - y$  plane which is depicted by dotted lines in Fig. 1.6. Moreover, each particle touches the solenoid axis just once and returns to its circular trajectory. After some time and a certain distance the particles move on their trajectories to new spots. The new positions of the particles are marked as  $A', B', C', D'$ . For better understanding there is also a particle  $E$  which is not situated on the beam surface at the beginning and its new position  $E'$  is in the volume of the new *focused* beam shown as a dashed circle. The radius of the original beam decreases from  $OA$  to  $OA'$ . This is the main process of periodic focusing in a uniform magnetic field.

In my previous work [9], the using of magnetic solenoid is demonstrated with the help of numerical simulations. A simple matlab program modeling a charged particle beam trajectories and computing emittances in the solenoid was developed. In this matlab code, the trajectories are calculated by equations of motion of charged particles in the magnetic field of solenoid. Based on the knowledge of initial particle beam emittance, a set of particles in the phase space was generated by a random function. Then, the system of three differential equations of motion in cylindrical coordinates are solved for initialized particles:

$$m(\ddot{r} - r\dot{\theta}^2) = er\dot{\theta}B_z \quad \text{focusing,} \quad (1.33)$$

$$m(2\dot{r}\dot{\theta} + r\ddot{\theta}) = e(\dot{z}B_r - \dot{r}B_z) \quad \text{rotation,} \quad (1.34)$$

$$m\ddot{z} = -er\dot{\theta}B_r \quad \text{acceleration.} \quad (1.35)$$

The results of the simulation are shown in Fig. 1.7. In this case, the beam of 100 protons is initialized with emittance  $0.5 \pi \cdot \text{mm} \cdot \text{mrad}$ . Then, the beam is moving in the magnetic field of solenoid along z-axis. The length of solenoid is 15 cm and the magnetic field in the centre of solenoid is set to 17.2 T.

In the simulation, a focused beam of protons was observed at z-distance about 35 cm from the front edge of the solenoid. At later stage of the beam propagation in solenoid, the beam is again divergent. However, if the magnetic field and the length of the solenoid would be setup properly, divergence of initial proton beam could be decreased.

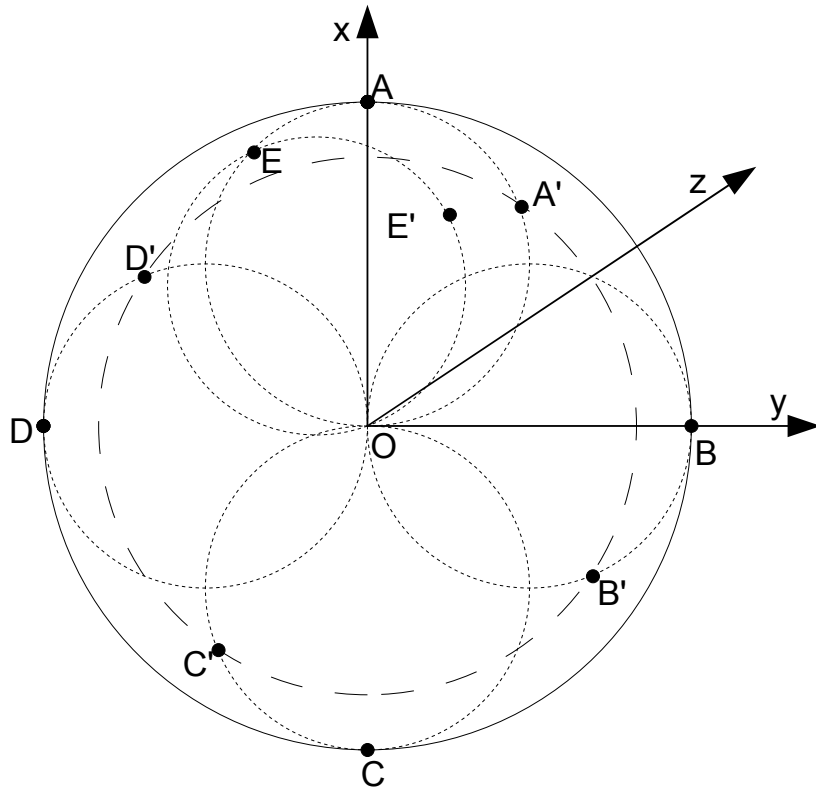


Figure 1.6: Focusing in the region with a uniform magnetic field;  $A, B, C, D, E$  – particles' positions at the beginning,  $A', B', C', D', E'$  – particles' positions after focusing,  $O$  – the centre of the beam; [39]

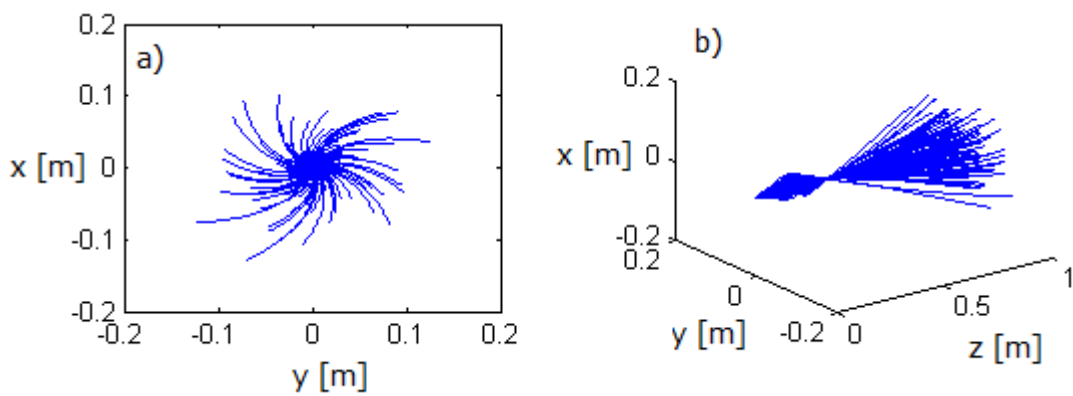


Figure 1.7: Examples of spatial views of charged particle beam trajectories in magnetic field of solenoid; a) y-x plane, b) 3D graph; Parameters of the beam: 100 protons, initial emittance  $0.5 \pi \cdot \text{mm} \cdot \text{mrad}$  initial magnetic field in the solenoid centre 17.2 T, focus at 0.35 m

## Quadrupole magnets

Quadrupole magnets (PMQs) are very strong focusing magnets arranged in quadrature, i.e. they are rotated  $90^\circ$  from each other and spaced-apart by electrical insulators, Fig. 1.8. In fact, PMQs are used for making particle beams more convergent when they move through.

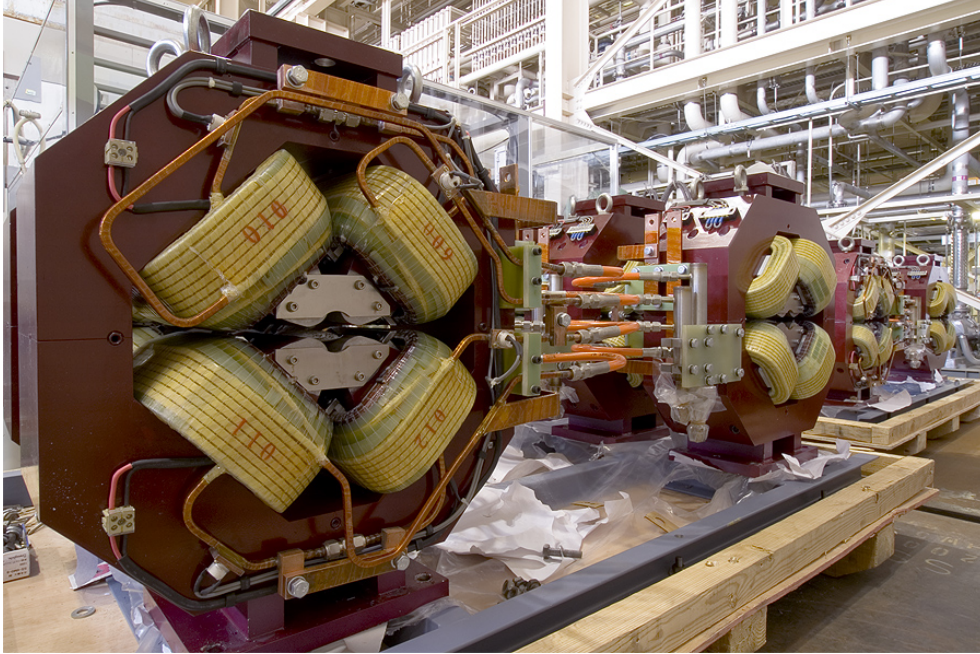


Figure 1.8: A batch of quadrupole magnets built for ATF2 by collaborators at IHEP, Beijing; [40]

The miniature permanent quadrupole magnets with small acceptance angles are components which decrease divergence and, unlike curved targets, could be used for high repetition rate operations [6]. Focusing of a stable, at 1 Hz repetition-rated, laser-driven 2.4 MeV proton source using Ti:sapphire laser system and conventional PMQ pair is demonstrated in Ref. [6]. The proton beam is focused at the distance of 650 mm from source with focal spot of  $\sim 3 \times 8 \text{ mm}^2$ . Moreover, the results are confirmed with Monte Carlo particle trajectory simulation.

## Conical cavity target holder

A divergence decreasing method using a target holder with an array of conical cavities is reported in Ref. [7]. The cavity is used for inducing an electric field. Thus, protons emitted from the target are collimated when they are traveling through the cavity. The holder used in experiment on J-KAREN Ti:sapphire laser system at Japan Atomic Energy Agency is made from aluminium and contains 16 conical cavities by 4 mm spacing arranged in a row. Moreover, the results obtained with conical target holder does not depend significantly on the target material or thickness. In addition, the conical cavities are not destroyed by the laser pulse, which is its great advantage from practical point of view, because only the foil target have to be replaced after laser shots. This target holder and whole experimental set-up can be seen in Fig. 1.9.

Numerous of hot electrons are emitted from the surface of the target holder during the laser pulse-holder interaction and leave the holder charged. A strong electric potential grows and enlarges over the surface with relativistic velocity. Then, created electric field has a component normal to the surface which finally leads to collimated protons with certain energies. The focusing strength of an electrostatic lens changes substantially with the beam energy.

As a result, a 7 MeV proton beam of more than  $10^6$  particles have been collimated to 16 mrad by focusing 2 J, 60 fs Ti:sapphire laser onto targets from different materials (Al,  $\text{Si}_3\text{N}_4$ ), [7]. Unfortunately, the obtained values are too low for hadron therapy treatment which requires a well collimated  $\sim 200$  MeV proton beam. In theory, if ten times stronger collimating electric field will be applied within the volume of the conical cavity with the same size of the target but with a three times greater height, the well collimated 200 MeV proton beam will be obtain at 5 cm away from the target [7].

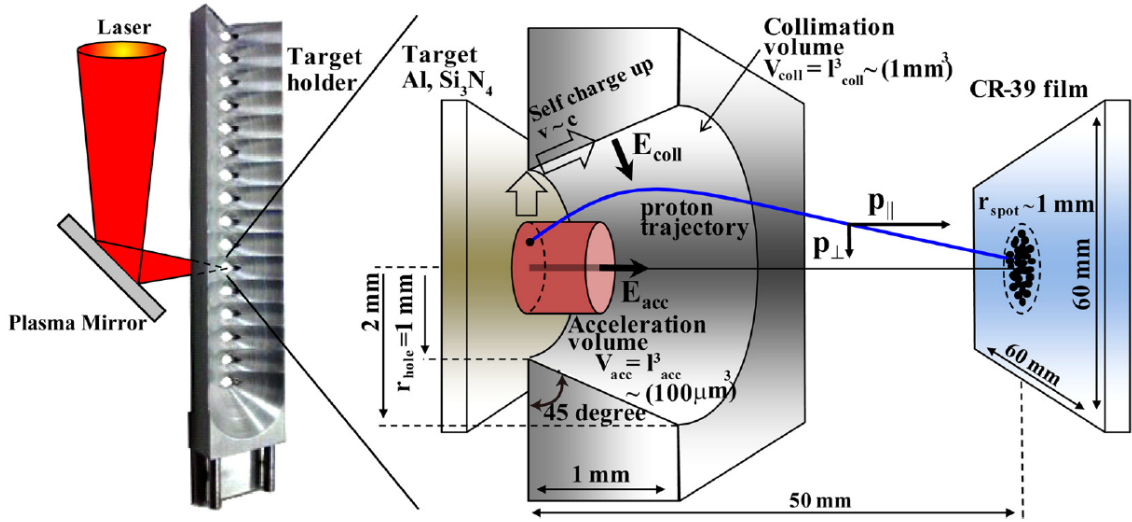


Figure 1.9: Experimental setup. Whole view of the target holder and cut away view of one of the conical cavities in the target holder arranged in a row are shown. The distribution of the static electric fields for acceleration ( $E_{acc}$ ) and collimating ( $E_{coll}$ ); [7]

### 1.4.3 Decreasing beam divergence in the ultra-intense short pulse regime

It was shown experimentally that divergence of proton beams accelerated during ultra-intense laser irradiation of thin foils can be influenced by varying laser contrast. The laser contrast is the ratio of the main pulse intensity to that of the nanosecond amplified spontaneous emission (pre-pulse). Thus, the careful control of the laser contrast is crucial in laser-driven ion applications. A surprising decrease from  $20^\circ$  to  $10^\circ$  is observed when the increasing laser contrast using a double plasma mirror system is used (contrast was increased by a factor of  $\sim 10^3$ ). Moreover, the improved collimation persisted over a various thickness of targets (from 50 nm to  $6 \mu\text{m}$ ); the increased flux was measured with thinner targets (50 nm) [8].

Naturally, the properties of laser-driven ion beams are influenced by the parameters of the laser such as pulse duration, intensity or energy. With increasing laser intensity, the effect of pre-pulses and amplified spontaneous emission become more significant. The aim of experiments is to have the pre-pulse as low as it is possible in contrast to the peak of laser intensity, because

the pre-pulse may destroy ultrathin targets which seems to be favorable for the most efficient acceleration of ions [41].

Hydrodynamics and 2D PIC simulations demonstrate that the key factor in altering the proton beam emission profile is a change in the fast electron generation process due to the pre-plasma presence. In the case of high contrast (i.e. short scale length  $\sim 1/4\lambda$ ), fluctuations in divergence is observed with varying target thickness ( $6 - 20 \mu\text{m}$ ), however, in low contrast (i.e. long scale length pre-plasma  $\sim 5\lambda$ ) case the divergence stays constant over two orders of magnitude in target thickness. In Fig. 1.10, the spatial profile of the accelerating longitudinal field along the rear surface after the peak of the acceleration is demonstrated. The profile is clearly different in the case of high and low laser contrast. For the low contrast case, the curvature is significantly lower and the protons from a significantly larger transverse region on the rear surface are accelerated by the sheath. In the case of the high laser contrast, at the beginning there is a high electron density which, as time goes on, results in a on axis peaked field where only protons within a few focal spots are accelerated to the highest energies [8].

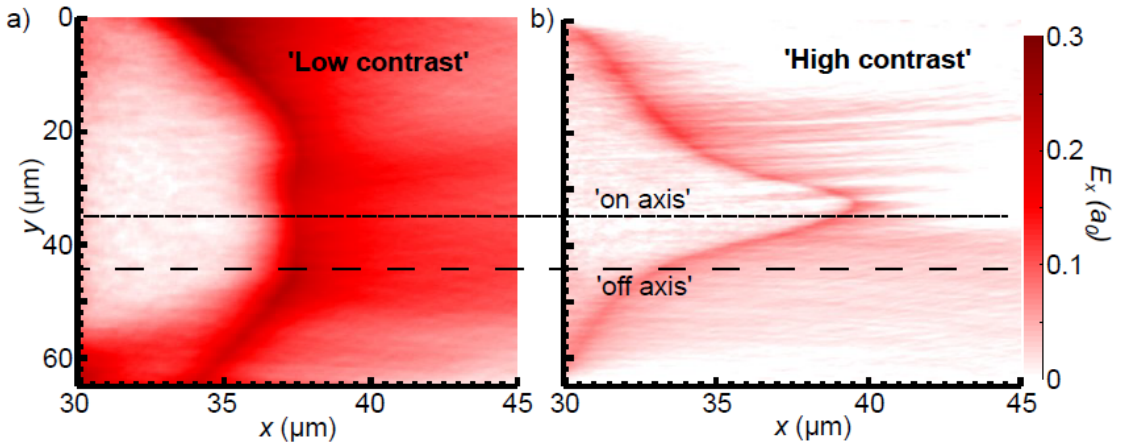


Figure 1.10: a) and b)  $E_x$  field spatial profiles along the rear surface showing the difference in sheath evolution between high and low contrast cases at  $t_{sim} = 320$  fs, i.e.  $\sim 200$  fs after interaction of laser pulse (end of the simulation in  $t_{end} = 450$  fs); [8]

## Chapter 2

# Applications of laser-accelerated ion beams

Laser-driven ion beams have a great importance in a number of technological applications since the high peak power pulsed lasers were developed. Nowadays, the research is focused on increasing the energy and decreasing divergence and energy spread of such beams. They can be a very promising source in medicine, for example for short-lived isotope production (positron emission tomography, PET), radiotherapy or hadrontherapy for treating malign tumors [42], [43]. Nevertheless, applications do not cover only biophysics, but also triggering and control of nuclear reactions, production and probing of warm dense matter [44], fast ignition of fusion targets [45], [46] etc.

Laser-driven ion beams will be highly investigated at Extreme Light Infrastructure (ELI) which is a new type of European large scale laser infrastructure specifically designed to produce the highest peak power (10 PW) and focused intensity ( $> 10^{23}$  W/cm<sup>2</sup>) [47]. In the Czech Republic, ELI-Beamlines project will be focused on many scientific field such as X-ray sources, particle sources, exotic physics, plasma physics and Multidisciplinary Applications of laser-Ion Acceleration (ELIMAIA beamline). An International Network called ELI-Beamlines MEDical and multidisciplinary applications (ELIMED) has the long term goal to demonstrate the potential future applicability (proof-of-principle) of laser accelerated ion beams in hadrontherapy, thus radiobiological studies will be exclusively dedicated to evaluate the biological feasibility [48]. In these days, ELIMED is being developed also covering preliminary studies for targets, beam handling, dosimetric delivering systems and radiobiology with laser-driven particles. Moreover, it is necessary to compare the biological effects of laser-driven ion beams (short bunches with very high dose rates) with those coming from "conventional" accelerators [49], [9].

### 2.1 Hadrontherapy

The applications of laser-driven ion beams are common not only in engineering and more technically oriented science but also in radiation physics and medicine. Strongly interacting particles are used in hadrontherapy, which is a radiological technique dealing with treatment of cancerous tumors. Hadrontherapy acts with protons (better dose distributions), neutrons (better tumor killing), pions or ions ( $\alpha$ , C, B, Li). Although several hadrontherapy facilities

based on conventional acceleration machines are operational worldwide, laser-driven hadron-therapy centers are still not present since they do not fit within the strict radiological requirements yet (energy, energy spread, shot-to-shot reproducibility). A great effort is put into the development of physical and clinical parameters suitable for effective and safe running of such treatment centers, since the laser-driven approach can drastically reduce the size of gantries and as a consequence the cost of future hadron therapy centers. Thus, they would be generally much more affordable than current hadrontherapy centers based on conventional accelerators. Studies on the biological effect of laser-driven ions on living cells have already been abundantly performed.

### Bragg peak

The enormous advantage of using protons or ions for cancer treatment is their energy deposition property. In contrast with X-rays (photons), protons show an increasing energy deposition with the growth of the penetration distance. The energy deposition remains steady in relatively lower penetration depths and, near the end of the particle trajectory, is followed by a sharp increase leading to the maximum of energy deposit – the Bragg peak [9]. This dependence is shown in Fig. 2.1.

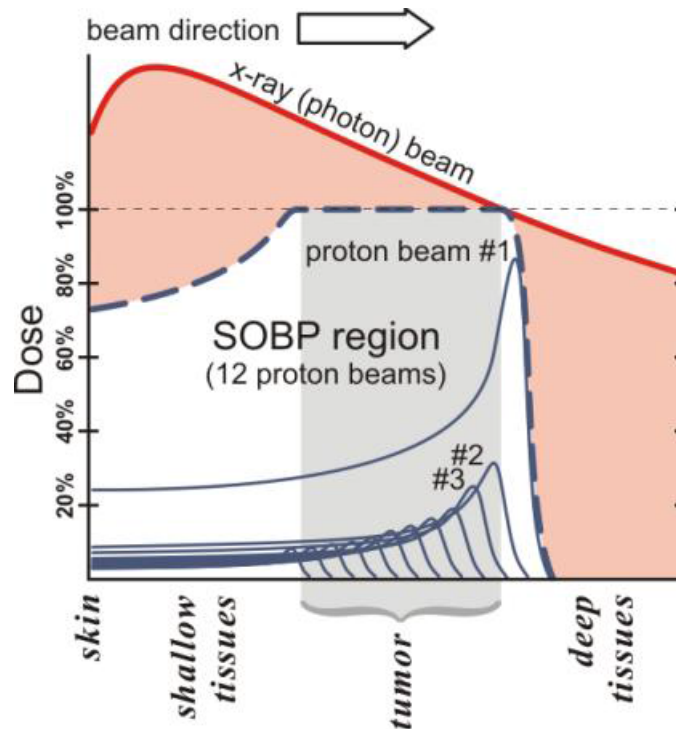


Figure 2.1: Dependence of typical dose deposition on penetration depth for both proton and photon beams. A proton beam can be precisely shaped (in three dimensions) to fit to the area of tumor. Making the area of maximum relative dose in required depth wider consists of putting together more energy deposition curves with different space-position of their Bragg peak. Compared to proton beams, photon beams have greater dose on healthy tissue in front of and behind the tumor; [50]

This characteristic allows minimization of the effect on the surrounding healthy tissue, while only the tumor is being treated. In fact, protons are losing their energy in atomic or nuclear interactions and they slow down faster than photons, because of their non-zero mass. The decreasing energy of protons allows greater interactions with orbit electrons, which, finally, causes the increasing energy losses. Obviously the maximum interaction with electrons appears at the end of the range noted as Bragg peak. In other words, the protons deposit more energy when they are slowing down (i.e., they have more time to experience the Coulomb interaction) and this energy is culminated in the Bragg peak [51]. An example how to cover the whole tumour volume is presented in Fig. 2.1. A proton beam can be precisely shaped ( $\sim \mu\text{m}$  accuracy [50]) in three dimensions to fit to the area of tumor. The idea consists in putting together more energy deposition curves with different space-position of their Bragg peaks to create a much wider peak. Moreover, the great advantage of this method is the possibility to use it near vital organs because of mentioned accuracy.

### 2.1.1 Suitable energies and required properties of the beam

Proton beams suitable for hadrontherapy have energies usually in the range of 60 – 250 MeV, where bigger energies means chance to destroy the tumor deeper seated in human body, and they are monoenergetic. Nevertheless, also beams with lower energy are utilized, for example in hadrontherapy center CATANA in Catania, Italy, a 62 MeV proton beam is used for eye tumor treatment.



Figure 2.2: left: CATANA proton therapy beamline – treating of eye tumor; right: using of implanted fiducials and tantalum clips (implanted under local or general anaesthesia) to make eye immobilized and add reference points in planning system before treatment; [50]

Moreover, proton beams utilized for cancer treatment have to be not only in the required

energy interval but also well-collimated and with a divergence as small as possible. Actually, this is one of the major drawbacks of laser-driven ion beams which have a typical half angle divergence up to  $30^\circ$ . Naturally, in medical practice the precision is a crucial requirement, thus, beams without sufficient narrow cross-section cannot be used.

Nowadays, more than 40 hadrontherapy centers have been built worldwide [52], but all of them are based on cyclotron/synchrotron concept, because laser-driven beams still do not fulfill all the physical, biological and clinical requirements.

### 2.1.2 Biological effects of ionizing radiation

The primary action of ionizing radiation on a tissue is the interaction between quanta of the radiation and the electron shell of atoms, rarely atomic nuclei. The result is the excitation and ionization of atoms, which may lead to physical changes, chemical reactions and in the case of living tissue to biochemical changes. These secondary effects can then lead to changes and damage of irradiated organism, or even to its demise – death.

There are many mechanisms of radiation action on living matter – e.g. free radicals or DNA damage.

Free radicals are formed when substances, containing especially water and complex compounds, are irradiated. As free radicals we note atoms and molecules having one or more unpaired electrons at the last orbit electron shell. Such atom or molecule is then highly unstable and reactive. Consequently, reactive radicals are able to cleave different types of internal molecular bonds in biomolecules by their oxidation and reducing effects and thus degrade their chemical structure required for appropriate biological function [53].

Nuclear deoxyribonucleic acid (DNA) is biochemically the most important macromolecule in the cell – basic information about the structure and function of cells are included there. Intervention in the biochemical structure of DNA can cause the end of cell necessary protein production, or changing "foreign" proteins. Ionizing radiation can cause an error in transmission of amino acids in the chain. Generally, radiation can cause many damages on the double helix of DNA. Two of the most frequent are single strand break (SSB) and double strand break (DSB). While SSB damages only one DNA sequence (the cell repairs such break usually easily), DSB affects both fibers of DNA (correction is much more difficult and often unsuccessful here). The damage of two DNA fibers often leads to cell death – direct or indirect, otherwise the cell is somehow fixed by reparative processes. By term "indirect death" it is meant a cell suicide called apoptosis. In short, the cell kills itself when it recognizes that damage is too big to be repaired [2].

The process of the ionizing radiation effect on a living tissue takes place in four stages differing in their speed and type of ongoing processes [53] (Fig. 2.3):

1. Physical phase – quantum of ionizing radiation gives its energy to electrons in shell which results in ionization or excitation (and their cascade reactions). This phase is very rapid, i.e.  $10^{-16} - 10^{-14}$  s.
2. Physical-chemical phase – chemical bounds between atoms and molecules are disrupted by excitation and ionization. Secondary physical-chemical processes of ions interaction

with molecules occurs. In these processes molecules are dissociated and free radicals are formed. As well as previous phase this stadium is rapid – it takes  $10^{-14} - 10^{-10}$  s.

3. Chemical phase – the ions, radicals, excited atoms and other products react with biologically important organic molecules (they "attack" a molecule of DNA, RNA, enzymes, proteins) and change their composition and function. Typical disorders at the molecular level are breaks in the DNA molecule. This phase lasts from  $10^{-3}$  s to few of seconds.
4. Biological phase – molecular changes in biologically important substances (DNA, enzymes, proteins) may result in functional and morphological changes in cells, organs and the whole organism. The time length of this stage varies from a few seconds at the cellular level to years at the whole body level.

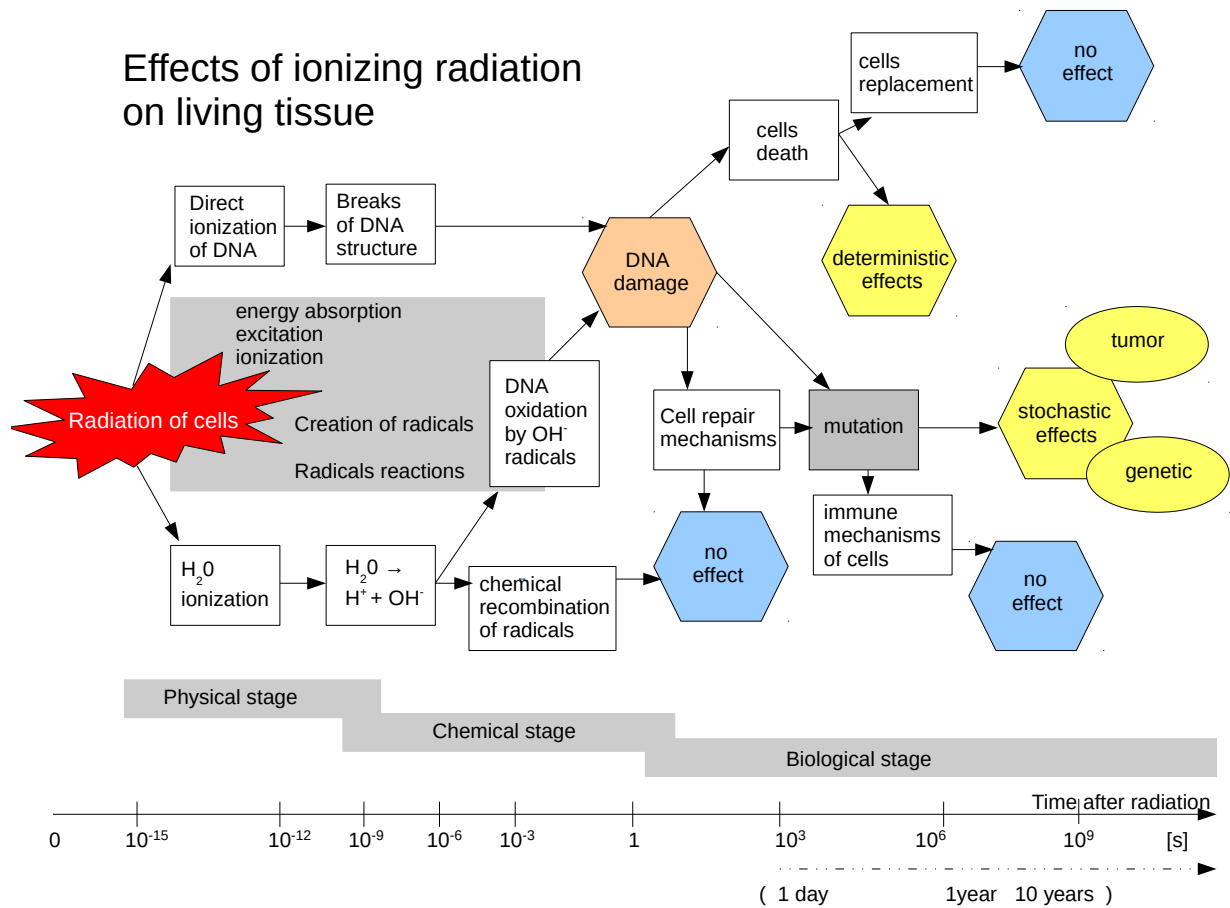


Figure 2.3: Effects of ionizing radiation on living tissue: schematic representation of important processes and their chronology

The physical and chemical stage are dependent on the physical parameters of the radiation, while the subsequent radiobiological reaction of cells is only determined by biological properties of the specific cell type. In Fig. 2.3 it is demonstrated that in the most cases of interaction of ionizing radiation with living tissues, the radiation has no effect. It is basically when [53]:

- the recombination of free radicals happens earlier than their reaction with biologically important substances
- the repair mechanisms successfully repair damaged DNA or other substances
- the cells killed by radiation are quickly replaced by other dividing cells
- the body immune mechanisms recognize and dispose genetically mutated cells

The effects of radiation on the organism (or in the case of hadron therapy, on the tumor) occurs primarily under the following circumstance:

- the tumor (organism) is irradiated with high-dose radiation, consequently several cells die and the tumor (body) is unable to compensate it.

### Important factors for determining cellular radiation effect

Dose and Linear Energy Transfer (LET) are the two main quantities that determine the biological effects induced by radiation. The dose to a cell can be characterized in sievert units, i.e. the average amount of energy deposited per unit mass within the cell [ $\text{J/kg}=\text{Sv}$ ] [2]. Typical survival-dose response curves can be found in Fig. 2.4. The second important quantity, LET, is described as the average amount of energy deposited along a unit length of the radiation particle path (e.g. proton) [2]. Another relevant variable is the Relative Biological Effectiveness (RBE) providing information about biological effectiveness of different types of ionizing radiation. RBE is usually plotted against LET with  $\gamma$ -rays or X-rays as standard types of radiation [2].

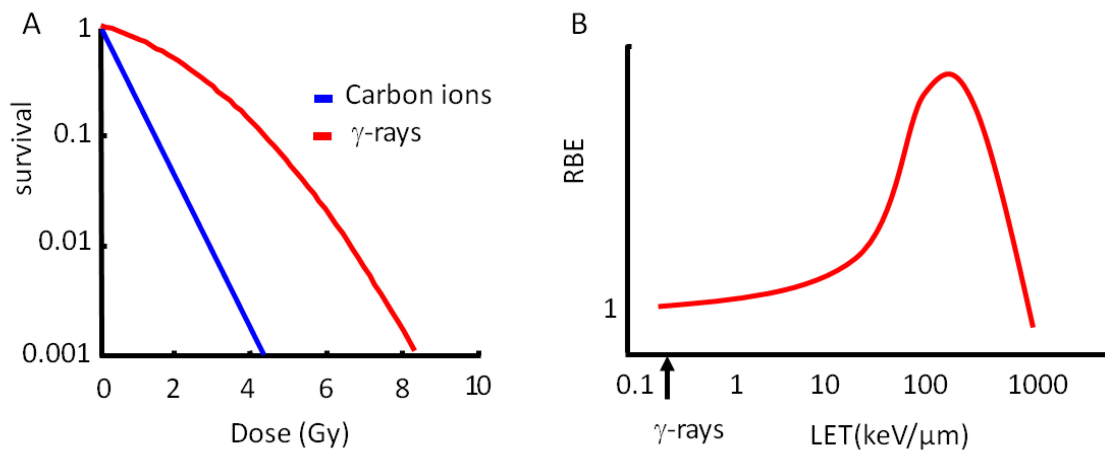


Figure 2.4: (A) Typical dose response curves of survival of cultured mammalian cells exposed to  $\gamma$ -rays and ion particles with LET of  $\sim 100 \text{ keV}/\mu$ , (B) Typical relative biological effectiveness – linear energy transfer (RBE-LET) relationship demonstrating that RBE peaks near  $100 - 200 \text{ keV}/\mu\text{m}$ ; [2]

## Difference between particle irradiation from laser-driven and conventional sources

The greatest difference between particle irradiation from laser-driven and conventional sources is the dose rate.

In the case of conventional accelerators (synchrotron, cyclotron), dose rates reach maximum limit 1 Gy/s (but can be as high as  $\sim 10^3$  Gy/s in the case of spot scanning mode). The total irradiation time of dose below 1 Gy/min spans from minutes to hours and "low dose rate effects" are observed. Such times are comparable to those of DNA repair, thus, a low dose rate effect is connected to the repair. Moreover, previous studies demonstrated that cellular radiosensitivity increases when cells are irradiated at such low dose rates [2].

In the case of laser-driven radiation, the dose rate is much higher than in previous case and can exceed  $10^9$  Gy/s with significantly shorter particle bunch length (typically  $\lesssim$  ns) [2]. Relatively fewer studies were written to a topic of ultra-high dose rates and this field is still under investigations. Nevertheless, it is very probable that if an ultra high dose rate effect exists it must be bounded with specific early time physical interactions (e.g. ionizations, excitations and radical generations). On the other hand, it was demonstrated that for an isolated cell, the effect of laser-driven radiation at an ultra-high dose rate does not likely differ from that of radiation at a moderate or a low dose rate generated by conventional accelerators [2].

## 2.2 Inertial confinement fusion

Energy production by thermonuclear fusion contains two main approaches. The first method is focused on magnetic confinement fusion (MCF), where tokamaks, stellarators and other magnetic devices are used. The second technique covers inertial confinement fusion (ICF) where lasers irradiating fuel capsules are included. The aim is to burn a few milligrams of fuel compressed to more than 1000 times liquid density within the time interval in which mass inertia keeps the burning fuel together. There are three stages independent to the driver and the irradiation regime - *implosion*, *ignition* and *burn* [54].

In the field of ICF, two approaches are under considerations:

- *direct* drive
- *indirect* drive

### 2.2.1 Direct drive

In *direct* drive ICF high power lasers are used to irradiate the surface of fuel capsule (usually made from deuterium and tritium) in order to ablate plastic surface and accelerate the fuel inward. To take a look on direct drive in more detail, we start with spherical implosion shown in Fig. 2.5.

#### Spherical implosion demonstrated on direct drive ICF case

Firstly, the fuel pellet is irradiated by laser (for example 22.7 ns long pulse of ultraviolet 0.25  $\mu$ m laser light is used). The best way to obtain uniform irradiation of capsule is to use large number of overlapping beams, focused by lenses placed at a distance of few meters from the capsule. The surface of fuel ball is made from plastic ablator with high atomic number Z. Under the shell, the thin layer of DT ice is placed followed by DT gas in the middle

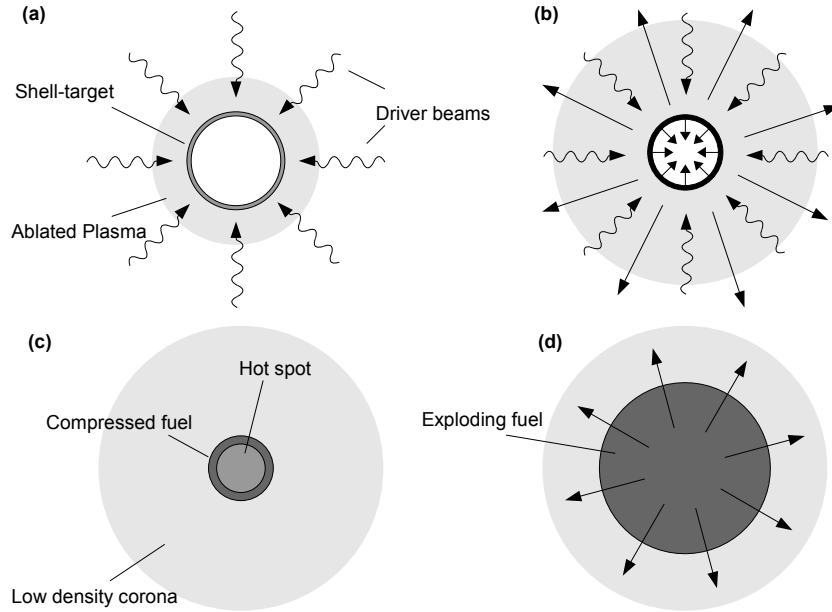


Figure 2.5: Four stages of spherical implosion; (a) ablation, (b) fuel implosion, (c) compressed fuel, ignition of hot spot, (d) explosion; [54]

of the pellet, see Fig. 2.6. Individual layers of heated surface is peeling off and ablating outwards. This phenomena creates the force which push the surface away from capsule. Then, as a result of momentum conservation forces, the second force, *ablation pressure*, with the same strength is formed in the opposite direction. Thus, non-ablated part of the capsule moves inwards under the action of the ablation pressure. Subsequent shocks now lead to smooth acceleration of the whole solid shell. Moreover, shockwaves are released gradually, but each subsequent wave has greater speed than previous one, so they coalesce at the same time and reach the center of the pellet. By this approach we obtain fast and nearly isentropic compression, which is much more higher than the compression with growing pressure (which is, in fact, asymptotically growing as  $p/p_0, \rho/\rho_0 \rightarrow 4$ ) [54]. The fuel is compressed to extremely high densities and heated by the sequence of shock waves to very high temperature. Then, hot spot is formed and ignited. A resulting burn wave is then running outwards, igniting the whole fuel, which expands rapidly.

## 2.2.2 Indirect drive

In *indirect* drive ICF, the fuel pellet is placed inside a hohlraum, i.e. a radiation confinement cavity [46]. The inner cavity walls are irradiated and heated by lasers, ion beams, or by x-rays from Z-pinch plasma in order to generate soft x-rays which, instead of laser itself in direct drive, will irradiate and ablate the fuel capsule. The resulting implosion is driven with much higher degree of symmetry which avoids many instabilities. On the other hand, conversion efficiency of driver energy into soft x-rays energy is still very low.

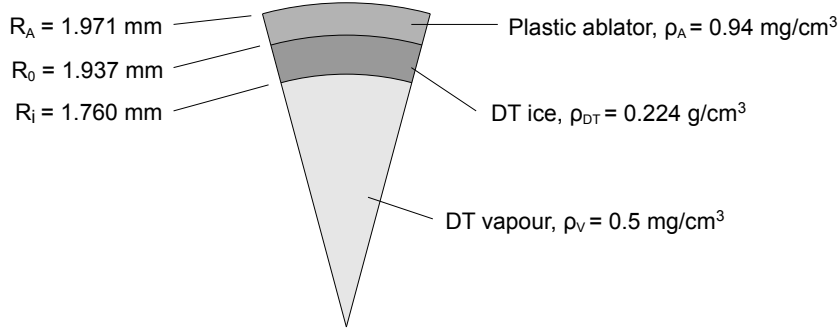


Figure 2.6: Fuel pellet used in ICF made from DT ice, DT vapour and plastic ablator with high Z number; [54]

### 2.2.3 Fast ignition

Fast ignition (FI) initiated by a laser-driven particle beam is used as a means to increase the gain, reduce the driver energy, and relax the symmetry requirements for compression (FI is believed to be independent of difficulties with hot spot ignition), mainly in direct drive ICF [46], [45]. The ignition requirements are following [45]:

- delivered power density  $\approx 10^{22}$  W/cm<sup>3</sup> (i.e.  $\sim 10$  kJ in  $\approx 20$  ps within a volume of linear dimension  $\approx 20$   $\mu$ m)
- DT fuel compressed to  $\sim 400$  g/cm<sup>3</sup>
- areal density  $\sim 2$  g/cm<sup>2</sup>

With using laser-driven proton beams, great advantages were brought in Fast ignition concept. A few scenarios are discussed below.

#### Fast ignition of ICF pellet in hohlraum by laser-driven ion beam

The great advantage of laser-driven proton beams used in fast ignition is that the protons can be produced and accelerated very rapidly to high energies up to tens of MeV in a few ps over a distance less than 100  $\mu$ m. This scenario allows to produce such beam very close to the fusion pellet.

A concept of fast ignition using laser-accelerated protons is shown in Fig. 2.8, where the indirect drive ICF geometry is used. Firstly, the spherical target attached to the hohlraum is irradiated by multiple petawatt-class laser beams (to obtain equally irradiated target surface, i.e. to prevent instabilities). Then, an intense proton or ion beam is accelerated from the rear side of the target. Moreover, this beam is well-focused because of the target shape decreasing a divergence of the beam. A thin metal window in the hohlraum wall protects the rear surface of the foil from preheat by the intense soft x-ray radiation. This radiation is generated

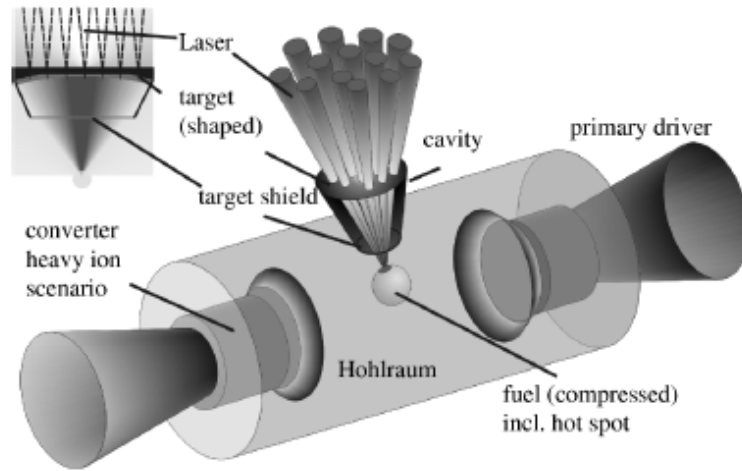


Figure 2.7: Indirectly driven FI using a laser accelerated proton beam (not to scale). The rear surface of the laser target is shaped to focus the ion beam into the spark volume; [46]

in the hohlraum by the implosion driver. Required distance for the proton acceleration is provided by vacuum gap between the target and the entry window. Once the protons penetrate this window they are taken as neutralized, because their space charge will be compensated by the plasma within the hohlraum. Energetic protons with high currents are focused ballistically into the hot spot and heat them to the ignition temperature  $kT \geq 10$  keV. The compression of the fuel must be fast and isochoric [46].

The main problems which scientists have to face are low conversion efficiency of laser light to energetic protons (few percent) and also high proton beam divergence which determines its focusability and thus influencing the final limit on the useful proton energy range.

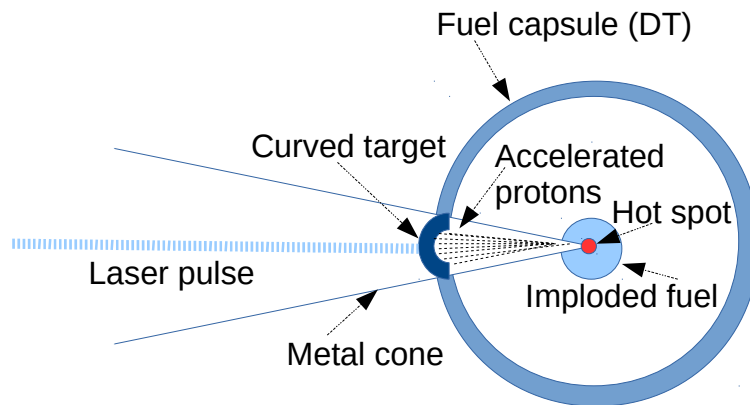


Figure 2.8: Proton-driven fast ignition concept with metal cone based on TNSA proton acceleration

### Fast ignition of ICF capsules with reentrant cones by laser-driven ion beam

ICF capsules with reentrant cones (see Fig. 2.8 and Fig. 2.9) were developed in order to reduce difficulties with delivering the short-pulse laser into the overdense plasma and the electrons into the dense fuel in direct drive approach. As a required consequence the path leading to the DT-core of the capsule stays cleaner in contrast to other scenarios [45].

Nowadays, the most favorable approach is to produce the proton beam from concave curved target [55] (smaller divergence in contrast to e.g. flat foils) via Target Normal Sheath Acceleration (TNSA) scenario and to focus it by metal cones [56]. In this scenario a high-intensity ( $< 10^{20} \text{ Wcm}^{-2}$ ) laser irradiates a foil which is placed usually in metal cone, distinct and external to the fuel capsule. Accelerated laser-driven ion beam is generated due to laser-target interaction and then it is focused onto the fuel to rise its temperature and ignite it. The main problem of this approach is that the beam cannot be created too far from the fuel, because it would be spread both in space and time and the density would decrease under the limit required for ignition [45].

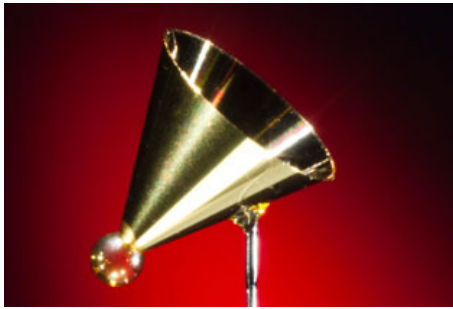


Figure 2.9: Cone-in-shell target: target with a plastic spherical shell of diameter  $860 \mu\text{m}$ , and a gold cone with an opening diameter of  $3.5 \text{ mm}$ , is used to study the Rayleigh-Taylor instability in spherical implosions; [57]

### Fast ignition and heavier ion beams

A few years ago great opportunities for FI associated with generation of heavier ions were appeared. The first achievement was the experiment on Trident when quasi-monoenergetic laser-driven C-ion beams generated from layered microstructured foil targets were demonstrated [58]. Nevertheless, FI with heavier ions requires significantly higher energy than protons in order to penetrate the fuel capsule sufficiently deep [45]. This problem might be solved by using a new accelerating scenario acting for high intensities ( $\sim 10^{20} - 10^{21} \text{ Wcm}^{-2}$ ) named Break-Out Afterburner (BOA) described in sub-chapter 1.2.4. BOA looks promising for FI concept with producing C-ion beams which are quasi-monoenergetic (energy spread  $\sim 10\%$ ) and having energies  $\sim 0.5 \text{ GeV}$  at reasonable efficiency ( $\sim 10\%$ ) [45]. Nevertheless, we have still insufficient knowledge to optimize such beams in an IFE devices (i.e. power plants).

## Chapter 3

# Particle-in-cell simulations of angular distribution of accelerated protons from advanced targets

### 3.1 Plasma modelling

There are three main possible descriptions in plasma modeling – Kinetic, Particle and Hydrodynamic description. Single particle description is used for the plasma with strong external field when the detailed knowledge of involved physical processes is crucial. On the other hand, for a system with a large particle number it is neither possible nor desirable to determine the motion of every single particle and, thus, kinetic description, using statistical approach with average macroscopic properties, is applied. The advantage of statistical approach is that no knowledge of individual particle motion is required to describe observable phenomena [59], [60]. Finally in the hydrodynamic approach, plasma is described via macroscopic parameters and equations for the system are obtained by taking velocity moments of the Boltzmann transport equation. This modeling approach is faster than the previous two, but the results are less accurate. Hydrodynamic approach can be used only when the assumption of local thermodynamic equilibrium is fulfilled.

- **Kinetic description** – Kinetic model deals with general distribution function  $f_\alpha(t, x_\alpha, v_\alpha)$ , where index  $\alpha$  means particle species. Boltzmann transport equation (BTR) is the equation describing a time evolution of the general distribution function  $f_\alpha(t, \vec{x}, \vec{v}_\alpha)$ . It can be derived with assumption of  $\alpha$ -particles collisions with target from  $\beta$ -particles [11]:

$$\frac{df_\alpha(t, \vec{x}, \vec{v}_\alpha)}{dt} = \sum_{\beta} S_{\alpha\beta}, \quad (3.1)$$

where right side is called Boltzmann collision integral. The commonly used BTR equation has the form:

$$\frac{\partial f_\alpha}{\partial t} + \left( \vec{v}_\alpha \cdot \vec{\nabla}_x \right) f_\alpha + \frac{1}{m_\alpha} \left( \vec{F}_\alpha \cdot \vec{\nabla}_v \right) f_\alpha = \sum_{\beta} S_{\alpha\beta}. \quad (3.2)$$

The right side express the collisional term which vary for different approaches to collisions. The resulting equations are called Fokker-Planck, Landau, Boltzman, BGK

(Bhatnagar-Gross-Krook) or Vlasov equation [11]. The last case is suitable for collisionless plasma, i.e. the low temperature plasma where collisions are negligible. Thus, the collision term in BGK is zero:

$$\frac{\partial f_\alpha}{\partial t} + \left( \vec{v}_\alpha \cdot \vec{\nabla}_x \right) f_\alpha + \frac{1}{m_\alpha} \left( \vec{F}_\alpha \cdot \vec{\nabla}_v \right) f_\alpha = 0. \quad (3.3)$$

- **Particle description** – Plasma is a system of single charged and neutral particles in vacuum. The plasma is described by electrons and ions moving under the influence of electric and magnetic field (due to their own charge) and of laser field [13]. Electromagnetic field is described via Maxwell equations for electric field  $\vec{E}$  and magnetic field  $\vec{B}$ :

$$\nabla \times \vec{E} + \frac{\partial \vec{B}}{\partial t} = 0, \quad \nabla \cdot \vec{B} = 0, \quad (3.4)$$

$$\nabla \times \vec{B} - \varepsilon_0 \mu_0 \frac{\partial \vec{E}}{\partial t} = \mu_0 \vec{j}, \quad \nabla \cdot \vec{E} = \frac{\rho}{\varepsilon_0}, \quad (3.5)$$

where  $\vec{j}$  is current density,  $\varepsilon_0$  is permittivity,  $\mu_0$  is permeability and  $\rho$  is charge density. For practical reasons, computer simulations of plasma using particle codes are limited to  $N \approx 10^8$  particles, but the typical value for laboratory laser-plasma is  $N \approx 10^{15}$  [13]. Thus, something as "simulation particle" called *macroparticle* containing a large number of real particles is presented. However, the decreasing number of particles means increasing noise.

- **Hydrodynamic description** – For hydrodynamic description not only Maxwell equations, conservation laws of mass, momentum and energy, but also equations of state are required. Moreover, a state of local thermodynamic equilibrium is assumed. Taking plasma as a fluid is a good approximation for system with relatively low intensities ( $\approx 10^{15}$  W/cm<sup>2</sup>) and relatively long laser pulses (ns). Nevertheless, the model is not always valid because of an assumption of local thermodynamic equilibrium LTE (for instance, temperature and pressure can be defined only in LTE) [13].
- Another possibility is to use hybrid modeling or gyrokinetic description [59], [60].

## 3.2 Theoretical approach of Particle-in-cell (PIC) simulations

Particle-in-cell (PIC) simulation is one of the most favourite algorithm in plasma physics. In general, the greatest advantage of PIC code is that it is not computed in the regions where no particle is present. PIC is a hybrid simulation which means that particles are moving in space freely (but according to movement equation) and fields are known only in predefined grid junctions. Thus, particles interact not with all other particles but with mean field generating by particle ensemble. Denoting  $N$  as particle number in the simulation, this approach decreases computational cost from  $N^2$  to  $N \log N$ . In many simulations, each "particle" in PIC code (i.e. macroparticle) represents a huge amount of real particles [11]. PIC simulations do not contain collisions. Nevertheless, collisions of charged particles with neutrals can be added by a Monte Carlo method.

### 3.2.1 Vlasov method versus PIC method

Let's assume the Vlasov equation (3.3) with single-particle density  $f(\vec{r}, \vec{p})$ , where  $\vec{r}$  and  $\vec{p}$  are position vectors of the particle in phase space. Naturally, each of them has three components, thus, we have to solve Vlasov equation in six-dimensional phase space, which is very computational-demanding even for 1D. Usually, finite differences on the Eulerian grid is used for solving the partial differential equation of Vlasov.

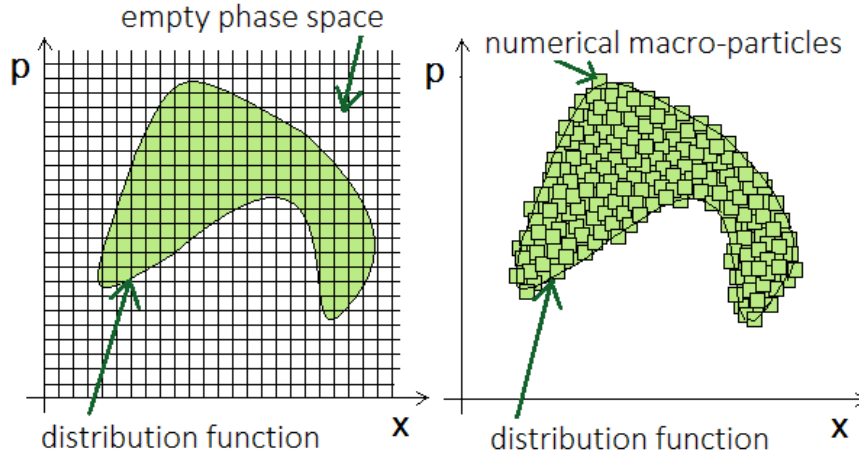


Figure 3.1: (left) Vlasov method: distribution function on Eulerian grid in 2D phase space; (right) PIC method: numerical macroparticles sample the distribution function

The reason of wasting so much computational effort and cost is clear from Fig. 3.1, where one plane of phase space with distribution function is shown. This distribution function is non-zero in dashed cloud, which represents the amount of phase space occupied by plasma particles and conversely zero in clear white surrounding space, where any particle is present. Regardless of whether the particles are in the region or not, all cells of the grid are included in numerical solving, which explains so high demands to computational power. Moreover, the impropriety of this computational approach rises with each dimension, because the empty space become bigger and bigger. Thus, solving kinetic collisionless Vlasov equation in six-dimensional phase space is almost impossible. On the other hand, there is one indisputable advantage of Vlasov codes and so the possibility of producing smooth results. This is mostly the reason why this codes are still studied.

Fortunately, there is a Particle-in-cell (PIC) method which can solve Vlasov equation more efficiently. To clarify it, we can see in Fig. 3.1 that the greatest advantage is approximation of distribution function by a set of finite phase-fluid elements (FPEE). Then the equation for distribution function is:

$$f_s(\vec{r}, \vec{p}) = \sum_k W_k S(\vec{r} - \vec{r}_k, \vec{p} - \vec{p}_k), \quad (3.6)$$

where  $W_k$  is the weight of  $k$ -th particle of species  $s$  and  $S(\vec{r} - \vec{r}_k, \vec{p} - \vec{p}_k)$  is the shape of particle in the phase space or the support function;  $\vec{r}$  is an observation point in phase space and  $\vec{r}_k$  is coordinate of the particle; for  $\vec{p}$  the same notation is valid. In fact, the shape

function is introduced, because real particles can occur anywhere in the space, but PIC simulation can compute the values of macro-quantities (i.e. particle density, current density) only in the node of the grid. Consequently, the real particles are assigned to simulation as macroparticles with specific *shape* (e.g. small squares in Fig. 3.1(b)). Moreover, the shape function has to satisfy the following conditions [61]:

- space isotropy,
- charge conservation,
- increasing accuracy (convergence) for higher-order terms.

As an example, the evaluation of the most simple shape function in 2D phase space can be given by:

$$S(x, p_x) = 1 \quad \text{for} \quad |x - x_k| < \frac{\Delta x}{2}, \quad |p - (p_x)_k| < \frac{\Delta p_x}{2}, \quad (3.7)$$

where  $\Delta x$  is width along  $x$  axis and  $\Delta p$  is width along  $p$  axis. In nutshell, when the real particle is inside examining cell with proportions  $\Delta x \times \Delta t$ , the shape function is equal to 1. Vlasov equation can be substituted by the following set of relativistic equations of motion for macroparticles [13]:

$$\frac{\partial \vec{r}_k}{\partial \vec{t}} = \frac{\vec{p}_k}{\gamma m_k}, \quad \frac{\partial \vec{p}_k}{\partial \vec{t}} = q_k \left( \vec{E}_k + \frac{\vec{p}_k}{\gamma m_k} \times \vec{B}_k \right), \quad \gamma = \sqrt{1 + \left( \frac{\vec{p}_k}{m_k c} \right)^2}, \quad (3.8)$$

where  $\vec{B}_k$  is magnetic field at the position of  $k$ -th particle, similarly  $\vec{E}_k$  is electric field in the same place,  $\gamma$  is relativistic factor and  $m_k$  is rest mass of  $k$ -th particle.

### 3.3 Basic four-step Particle-in-cell scheme (PIC)

A success of simulation is based on an appropriate choice of spatial and temporal step. In general, the time step of movement equation integrator should be significantly shorter than a period corresponding to electron plasma frequency. Moreover, the spatial step should be comparable to the Debye length in the simulated plasma system [11].

The basic cycle of PIC method has four steps as shown in Fig. 3.2, even if many of auxiliary procedures are needed for the final implementation of the PIC code.

#### Particle weighting, $(\vec{x}, \vec{v})_i \rightarrow (\rho, \vec{J})_i$

Charge and current densities in the grid nodes are derived from positions and velocities of particles. Each particle mass is divided between nodes according to well defined rule which ensures that the biggest part of the particle will belong to the closest mesh junction. Although in the same PIC cycle the same weighting order should be used, more orders exist and they, in fact, determine the quality and accuracy, but also the corresponding complexity, of the weighting [10]. After *Particle weighting* step, the source terms in Maxwell equations system (3.9) - (3.12) are known on the grid.

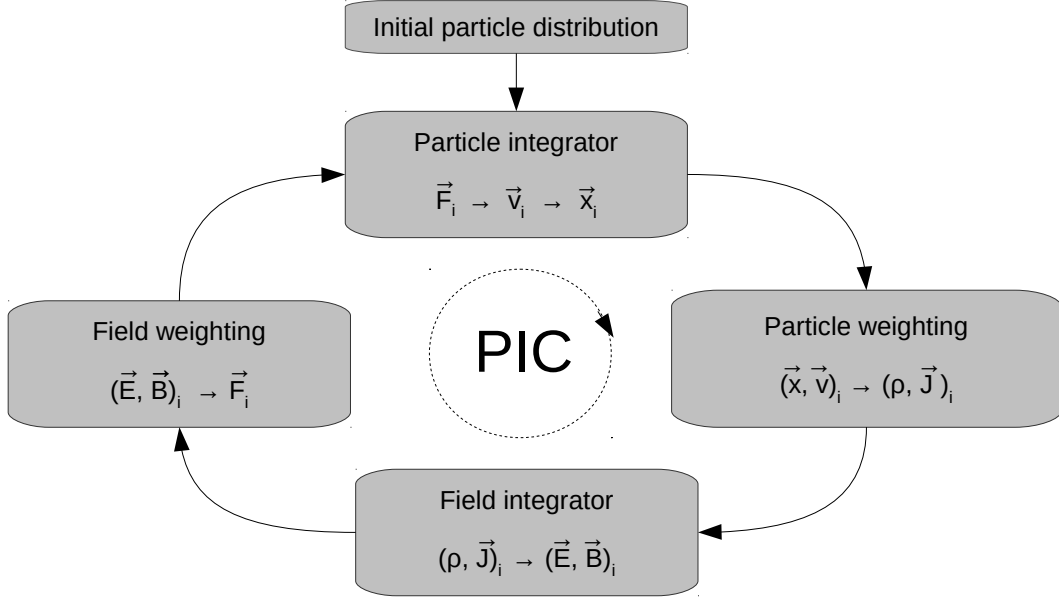


Figure 3.2: Basic cycled four-step scheme of Particle-in-cell method

**Field integrator,  $(\rho, \vec{J})_i \rightarrow (\vec{E}, \vec{B})_i$**

From the previous step, we know the source terms in Maxwell equations (3.9) - (3.12) and thus, we can obtain electric and magnetic fields  $\vec{E}$ ,  $\vec{B}$  on the grid.

$$\nabla \times \vec{E} = -\frac{\partial \vec{B}}{t}, \quad (3.9)$$

$$\nabla \times \vec{B} = \mu_0 \vec{J} + \frac{1}{c^2} \frac{\partial \vec{E}}{\partial t}, \quad (3.10)$$

$$\nabla \cdot \vec{E} = \frac{\rho}{\epsilon_0}, \quad (3.11)$$

$$\nabla \cdot \vec{B} = 0. \quad (3.12)$$

If the fields do not change much during one time step, they can be computed on the grid only from Poisson equation for potentials [11].

**Field weighting (interpolation),  $(\vec{E}, \vec{B})_i \rightarrow \vec{F}_i$**

Magnetic and electric fields on the grid obtained in previous step are weighted into particle positions. This is the opposite procedure to particle weighting presented before.

**Particle integrator,  $\vec{F}_i \rightarrow \vec{v}_i \rightarrow \vec{x}_i$**

Now, we know the fields in the location of the particles, i.e. we know the Lorentz force  $\vec{F}_i$ :

$$\vec{F}_i = \frac{d(\gamma \vec{v}_i)}{dt} = \frac{q}{m_i} \left( \vec{E}_i + \vec{v}_i \times \vec{B}_i \right). \quad (3.13)$$

Thus, we will get velocity  $\vec{v} = \frac{d\vec{x}}{dt}$  and then, position  $\vec{x}$ , by integration with respect to time. For the integration of equation of motion (3.13), Boris-Buneman and Leap Frog methods are usually employed [11], [62].

## 3.4 Computational background

### 3.4.1 Extendable PIC Open Collaboration (EPOCH)



Figure 3.3: EPOCH logo; [63]

EPOCH is a project to develop a UK community advance relativistic electromagnetic (EM) particle-in-cell (PIC) code written in Fortran. The code was published under the University of Warwick as a free full source code available for students and academic workers as CCP project <http://ccpforge.cse.rl.ac.uk/gf/project/epoch/> (sign-up is required). The core algorithm is developed by Dr. Chris Brandy and Dr. Keith Bennett at University of Warwick and based on the particle pusher and field update from Hartmut Ruhl's PSC code [63]. Moreover, there is a possibility to download well-written users or developers manual or share with others your helping comments & problems via discussion forum, which is actually one of the reasons why we decided to use EPOCH. The second reason was very user-friendly platform for setting input parameters. EPOCH is able to provide not only one-dimensional (1D) and two-dimensional (2D) simulations, but also three-dimensional (3D) simulations as well. For parallel computing the code needs MPI library (e.g. OpenMPI).

#### Input of parameters

Controlling of EPOCH code is user-friendly. For each simulation, one should create a new file called `input.deck`. In this file, the parameters of simulation are inserted and organized into different blocks. Most of them use The International System of Units (SI) (the exception is particle charge or mass which is set in multiples of electron charge or mass, respectively). Each block serves its own purpose – proportions of simulation area, laser parameters, particle species, fields, boundary conditions, output options, etc. In the EPOCH user manual, a very detailed interpretation of different parameters and their possibilities are reported. Moreover, a few examples of `input.deck` file together with starting package (code + manual) can be downloaded for better understanding.

#### Output files and Visualization

Output data are saved in user-defined time interval (which can be set as a parameter in `input.deck` file) of simulation into `.sdf` files (self-describing file). Then, these files can be loaded, plotted or visualized in Matlab or VisIt studio. In my experience, VisIt studio is better to first look on certain results, but Matlab provides more options to edit graphs and has more user-friendly interface. In distribution of EPOCH code there are also the `.sdf` Matlab functions for loading data (`*.sdf`) files generated during simulations with EPOCH code correctly.

### 3.4.2 MetaCentrum



Figure 3.4: MetaCentrum logo; [64]

2D or 3D PIC simulations are computational demanding for PCs. Thus, the simulation is usually prepared in personal computer and sent to the computing infrastructure (in our case called MetaCentrum) when the simulation is performed. Then, users are able to download computed data to their own computer.

Catch-all MetaCentrum Virtual Organization operates and manages distributed computing infrastructure consisting of computing and storage resources owned by CESNET as well as those of co-operative academic centers within the Czech Republic. The project tries to construct a virtual super-computer on which the tasks whose memory and/or CPU requirement are too severe could be solved. MetaCentrum membership is free for researchers and students of academic institutions in the Czech Republic, the members of the CESNET association, but including of the official appreciation formula to theirs publications is obliged [64].

MetaCentrum is used by different users doing their research in various areas such as computational chemistry, material and structural simulation, simulation of flow of gases and liquids, recognition and speech generation, physical geodesy, ecological modeling, video processing, data mining or analysis of medical images [64].

#### How it works in a few steps:

1. Use your name and password to login via `.ssh` client into MetaCentrum
2. Copy your simulation files that you prepared to your MetaCentrum account
3. Plan your job using the specification of requirements for computational resources
4. Wait until the job will not be done
5. Download the computed results into your computer
6. Visualize them by any tool, for instance Matlab or VisIt

To run simulations in MetaCentrum we must create a job and run it through the planning system PBS (Portable Batch System) (point (3)), which classifies jobs into queues according to the expected run time and to release the necessary computing resources for running the job. Simplified task could be defined in `.sh` script, e.g. `soubor.sh` as follows:

```
#!/bin/sh
#PBS -N curvedfoil
#PBS -q short
#PBS -l nodes=1:ppn=12:cl_minos
#PBS -l mem=1gb
#PBS -j oe
```

```

cd ./curvedfoil
module add openmpi-1.6-intel
echo Data | mpirun -np 12 ./bin/epoch2d

```

On the second line we set name of the job, on the third row we choose the queue (`-short` specifies maximum run time in the length of 1 hour), the fourth line is requesting 1 node (computer) having 12 processors (Minos cluster) and line 5 specifies the request of 1 GB of memory. Then, we move to the folder curved foil (line 8), which contains the file with epoch2d code and our input parameters file. Library for parallel computing is loaded on line 9. The job is added into MetaCentrum planning system by `-qsub` command in linux terminal.

Detailed description not only for setting of those parameters can be found on official MetaCentrum wiki page:

[https://wiki.metacentrum.cz/wiki/Scheduling\\_system\\_-\\_detailed\\_description](https://wiki.metacentrum.cz/wiki/Scheduling_system_-_detailed_description).

### 3.4.3 Implementation of Energy balance

In current version of EPOCH code (4.3.4), same as in the previous ones, energy balance and computing of absorption coefficient do not work well. Actually, energy balance is essential for initial check-up of simulation progress and both for the interpretation of results. Thus, the procedure how to get dimensionless energy balance [65] is described bellow in section 3.4.4.

### 3.4.4 Dimensionless energy balance

To obtain dimensionless equivalents  $\vec{E}'$ ,  $\vec{B}'$  (3.16) of electric and magnetic field  $\vec{E}$ ,  $\vec{B}$ , we have to specify its units and then multiply them by appropriate variables (electron charge  $e$ , electron mass  $m_e$ , laser angular frequency  $\omega$  and speed of light  $c$ ):

$$[E] = \frac{kg \cdot m}{A \cdot s^3}, \quad [B] = \frac{kg}{A \cdot s^2}, \quad (3.14)$$

$$[e] = A \cdot s, \quad [m_e] = kg, \quad [\omega] = s^{-1}, \quad [c] = m \cdot s^{-1}, \quad (3.15)$$

$$\frac{e\vec{E}}{m_e\omega c} =: \vec{E}', \quad \frac{e\vec{B}}{m_e\omega} =: \vec{B}', \quad (3.16)$$

$$[E'] = [-], \quad [B'] = [-]. \quad (3.17)$$

Then, dimensionless mass and charge is given by:

$$\frac{m}{m_e} =: m', \quad \frac{n}{n_c} =: n', \quad (3.18)$$

where  $n_c$  is critical density.

Total energy can be obtained by the sum of its particles and field part:

$$W_{field} = \frac{1}{2} \sum_{cell} ((E')^2 + (B')^2), \quad (3.19)$$

$$W_{particles}^i = \sum_{particles} m'_i \cdot n'_i \cdot (\gamma - 1), \quad (3.20)$$

$$W_{particles} = \sum_i W_{particles}^i, \quad (3.21)$$

$$W_{total} = W_{field} + W_{particles}, \quad (3.22)$$

where  $\gamma$  is relativistic factor given by:

$$\gamma = \sqrt{1 + \frac{\vec{p}_i^2}{m_i^2 c^2}}. \quad (3.23)$$

### 3.5 Setting of input parameters and target designs

Beam divergence is crucial parameter in characterizing laser driven ion beams. Many of ongoing or future applications highly depend on low angular spread to ensure their efficiency. This is the main motivation of preparing and testing various designs of target which can decrease divergence of laser driven ions beams. In the following Particle-in-cell (PIC) simulations, we use two-dimensional version of the EPOCH PIC code, where input parameters are set in the file called `input.deck`. All required details are sort in different blocks such as *control block* for setting of total time of the simulation, size and other properties of simulation area, *boundaries block* for setting of conditions on boundaries, *constant block* for defining frequently used constants or simple equations, *particle species block* for setting of amount of particles of each species, its mass, charge and other physical properties, *laser block* for setting the laser parameters and *output block* for setting the listing of output values.

#### 3.5.1 Various targets designs

In the simulations, we used the following targets demonstrated in Fig. 3.5: long flat foil (a), short flat foil (mass limited target) (b), foil with a hole on its rear side (c), foil with tiny microstructures on its rear side (d) and curved foil (e).

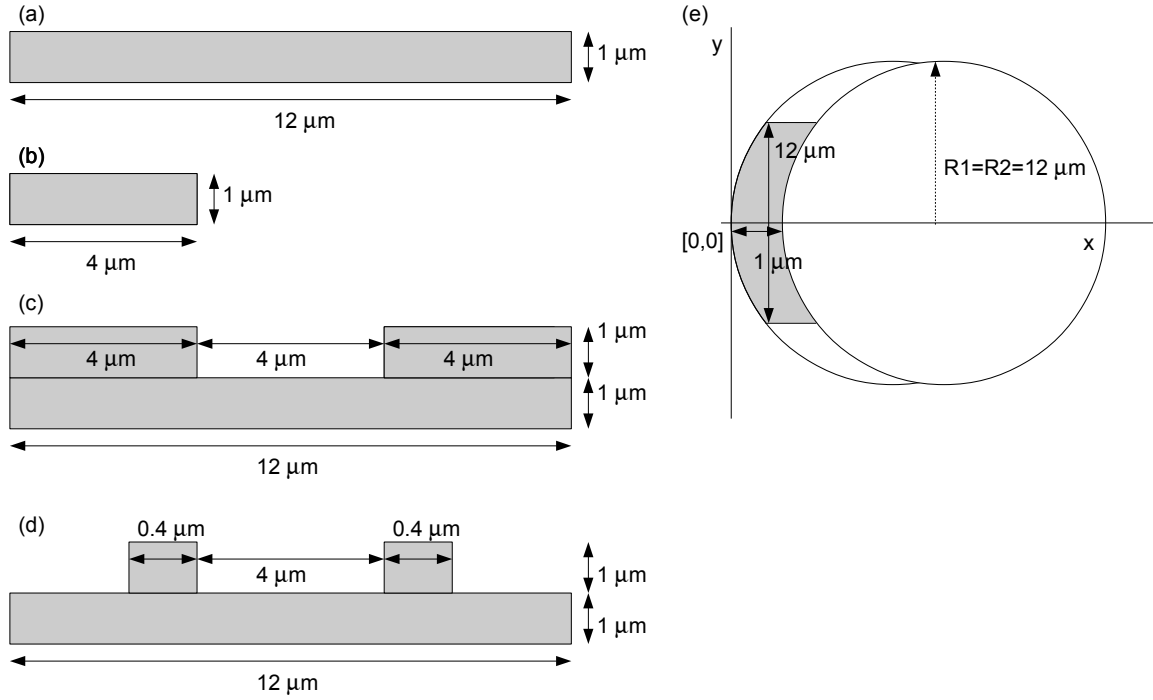


Figure 3.5: Schematic design of targets: (a) long flat foil, (b) short flat foil, (c) foil with a hole on its rear side, (d) foil with tiny microstructures on its rear side, (e) curved foil

### 3.5.2 Summary of simulation parameters

Main input parameters are listed below. For detailed description of the syntax and listing of input codes see [10].

- Simulation area is usually about  $30 \mu\text{m}$  long in the longitudinal direction (laser propagation direction) and about  $30 \mu\text{m}$  wide in the transverse direction with  $3800 \times 3800$  grid points. The only exception is the case of electrons spread display, where the simulation area is bigger – approximately  $70 \mu\text{m} \times 70 \mu\text{m}$ . The space around the target is not symmetric, i.e.  $\sim 13 \mu\text{m}$  in front of target and  $\sim 17 \mu\text{m}$  behind the target. More space behind the target is needed to study the physical phenomenas of proton acceleration from foil rear side (which is situated in the centre of the coordinate system).
- Laser peak intensity  $I = 4.5 \cdot 10^{20} \text{ Wcm}^{-2}$  (corresponding to the nowadays most powerful lasers)
- Laser wavelength  $\lambda = 800 \text{ nm}$
- Laser pulse time-profile has sinusoidal-square shape with full time duration 30 fs
- Laser beam has Gaussian spatial profile with beam width (in FWHM)  $2 \mu\text{m}$
- Laser beam has normal incidence to the target and comes along the x-axis in the positive direction

- Used particle species: electrons, protons and  $C^{4+}$  ions in ratio 1 : 1; quasineutrality conserved (carbon ions as well as protons have to be one fifth of electrons amount)
- Density of electrons in ionized target is  $n_{max} = 20 \cdot n_c = 3.5 \times 10^{22} \text{ cm}^{-3}$
- Simulated time of plasma evolution: 300 fs, outputs after each 15 fs (i.e. 20 times files for visualisation)

### 3.6 Density plots of expanding targets

Density plots of expanding targets at the end of the simulation help us e.g. to control simulation settings such as dimensions of the simulation area etc. and we can observe the basic trends of divergence. If we look at the expansion of ions, we can observe that carbon ions are forming smaller cloud than protons ( $C^{4+}$  ions are less accelerated than protons because of its lower  $q/m$  ratio). The crucial criteria of setting the simulation area dimensions is to lock all the protons inside the simulation box (and so the carbon ions), nevertheless a small part of electrons can leave the area (thus, kinetic energy of electrons (and total kinetic energy as well) will slightly decrease in the final energy balance plot). The reason why a small amount of the most energetic electrons can leave the simulation box is saving computational cost, when we observe ions primarily. Then, the quasineutrality is broken and other electrons are attached to expanding ions by electric force.

One might think that apparently a hole is formed in the target in Fig. 3.8 (here demonstrated on the curved one), but in reality this is not true as shown in Fig. 3.9 where the density of carbon ions is located in "the hole". The explanation is that protons are displaced backwards toward carbon ions.

In addition, comparison in the divergence tendency can be observed in Fig. 3.6 for target with a hole on its rear side and in Fig. 3.7 for target with tiny microstructures on its rear side. In the first case, we can see well collimated particle beam with the smallest simulated divergence (detailed explanation in chapter 3.7), in the second case there are three small bunches (finally connected to one) emitted from the thinner parts of the target (around the microstructures) which makes divergence larger.

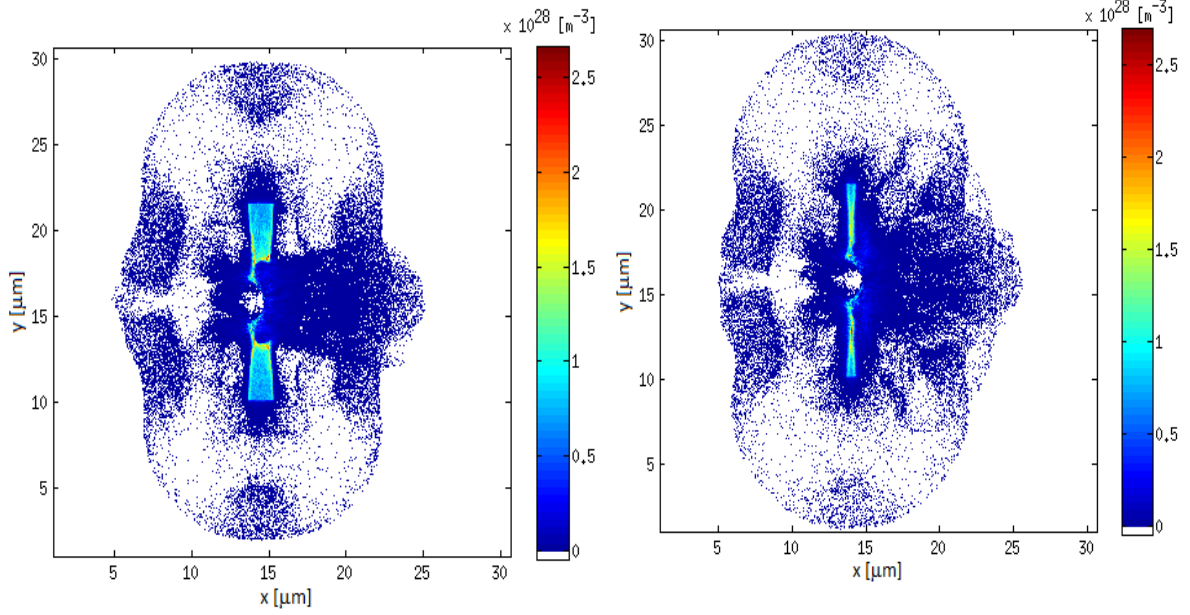


Figure 3.6: Density of protons in the foil with a hole on its rear side at the end of the simulation (300 fs, i.e. 240 fs after laser pulse interaction with target)

Figure 3.7: Density of protons in the foil with tiny microstructures on its rear side at the end of the simulation (300 fs, i.e. 240 fs after laser pulse interaction with target)

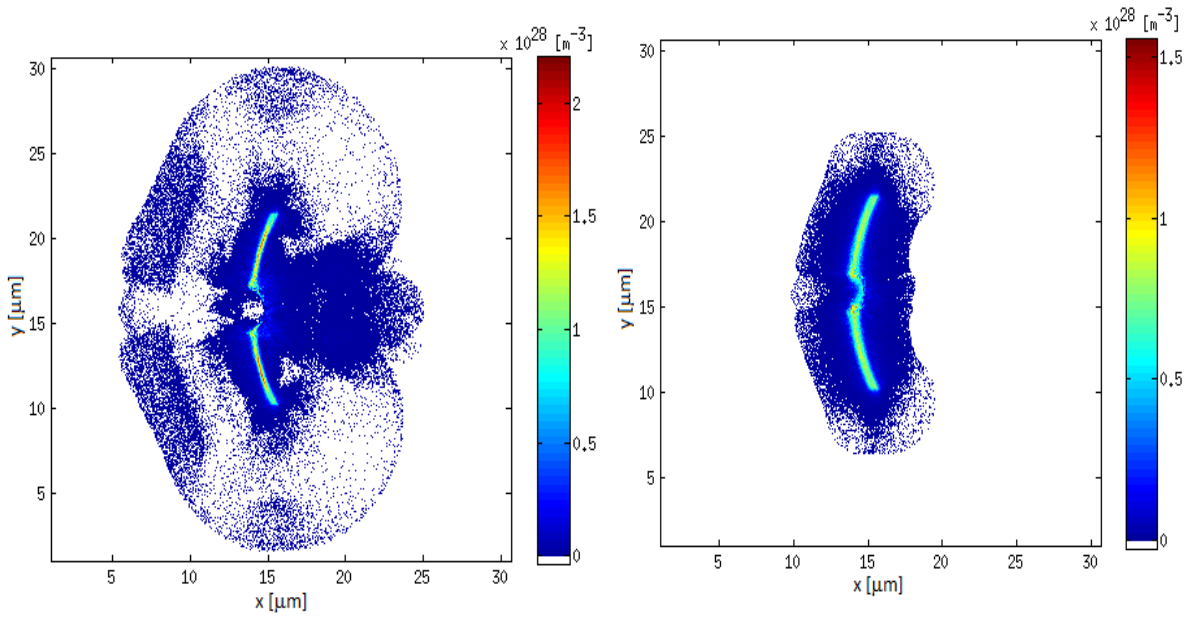


Figure 3.8: Density of protons in the curved foil at the end of the simulation (300 fs, i.e. 240 fs after laser pulse interaction with target)

Figure 3.9: Density of carbon ions in the curved foil at the end of the simulation (300 fs, i.e. 240 fs after laser pulse interaction with target)

### 3.7 Angular spread

A comparison between angular distributions of accelerated protons from all five designs of target is plotted in Fig. 3.10 and Fig. 3.11 for particles with energies above 10.0 MeV. For better clarity, the distributions are also split into smaller groups for plotting. All distributions are plotted at the end of the simulation, i.e. 240 fs after the start of the laser pulse interaction with the target. The energy interval above 10.0 MeV is taken because of showing the divergence of more energetic particles which are more suitable for possible applications, corresponding values for all target types are summarized in Tab. 3.1.

A brief overview of targets ranked by corresponding lowest divergence (e.i. from lowest to highest) is listed below:

- The *foil with a hole on its rear side* has the lowest divergence. Value of half angle proton divergence reaches  $\sim 9^\circ$  in FWHM for energies above 10.0 MeV. In fact, this result is in agreement with qualitative expectations that thicker parts of the foil can cut out the particles with high divergence on the sides of the beam, while the hole acts like "pre-defined path" when the accelerated beam can move quite freely (with lower divergence), and the rest of the foil is thick enough not to produce so much accelerated particles from its surface (the divergence stays low). Moreover, electrostatic field from sides of the hole also helps to sustain low beam divergence.
- The second most effective target to decrease the beam divergence is the *curved foil* which reaches  $11^\circ$  for energies above 10.0 MeV. Actually, the protons are accelerated perpendicularly to the surface from its rear side which is exactly the reason why more collimated protons are observed in the case of curved foil instead of flat foils (short and long). The reason why target with a hole on its rear side is better to decrease divergence than curved foil is that the protons are focused in a "point" (ideal case) quite rapidly in the case of curved foil and thus, they are also subsequently defocused. To reach lower divergence with curved foil, it is possible to put there for example a magnetic element to avoid the defocusing part. In contrast with curved foil, the proton beam accelerated from foil with a hole on its rear side has low divergence from the beginning and there is no big reason for defocusing.
- *Long flat foil* is used as reference target. It has no advantage in reducing the ion divergence.
- In the case of the *foil with tiny microstructures*, the foil does not end after the microstructures but continue to the length of long flat foil, thus, particles are accelerated also from these sides. This corresponds to three small bunches (see Fig. 3.7) which finally join together but with corresponding high divergence ( $13^\circ$  for accelerated protons; this value is almost independent on the proton energy).
- The largest divergence corresponds to the *short flat foil*. In fact, dimensions of the foil (length versus thickness) are quite similar, thus the laser pulse causes explosion of the foil which leads to significantly high divergence, higher than for the long flat foil.

Divergence usually decreases with increasing particle energy [66]. In fact, standard values of divergence for flat foils span from  $0^\circ$  to  $25^\circ$  in half angle as discussed in chapter 1.4. It

has to be also mentioned that proton beam divergence depends also on the time after the laser pulse interaction with the target, meaning that longer times, i.e. longer proton trajectory behind the target, correspond to higher divergences.

Similar values of proton beam angular divergence were also observed for protons with energies above 0.5 MeV. Most of the values were a few tenths of degree bigger which corresponds with previous the statement.

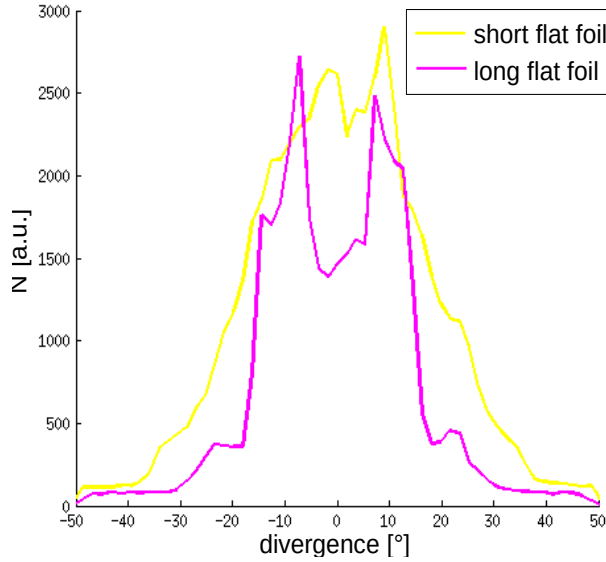


Figure 3.10: Energy from 10.0 MeV to maximum energy

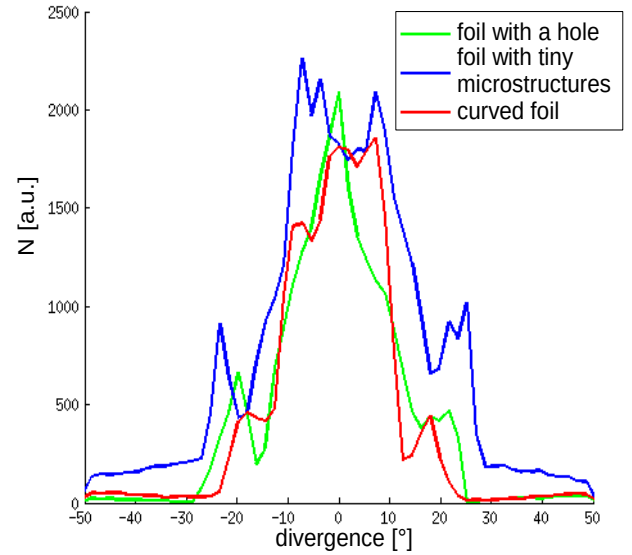


Figure 3.11: Energy from 10.0 MeV to maximum energy

type of foil	divergence of protons [°]
flat long	14.8
flat short	17.6
with a hole	9.4
tiny micro	13.3
curved	10.8

Table 3.1: Half angle divergence measured in FWHM for all target types; energy taken above 10.0 MeV

### 3.8 Energy spectrum

The comparison between energy spectrum of protons or  $C^{4+}$  ions for all five cases of simulated foils (long flat, short flat, curved, with tiny microstructures on its rear side and with a hole on its rear side) is shown in Fig. 3.12 for protons. The corresponding energy spectrum is created at the end of the simulation at the time 300 fs, i.e. 240 fs after the start of laser pulse interaction with the target. Maximum energies per atomic mass unit ( $u$ ) of each species (protons and carbon ions) are listed in Tab. 3.2.

type of foil	$E_{max}^{p+}$ [MeV]	$E_{max}^{C^{4+}}$ [MeV]
flat long	19.8	3.1
flat short	26.2	3.4
with a hole	19.4	2.5
tiny micro	20.9	3.0
curved	18.8	2.6

Table 3.2: Maximum energy of accelerated particles – protons ( $E_{max}^{p+}$ ) and carbon ions ( $E_{max}^{C^{4+}}$ ) for all target types

Maximum energies of protons as well as of carbon ions do not differ much for all target designs except short flat foil which shows a little higher energy for all particle species. Absorption coefficients for all targets are evaluated in Energy balance results (section 3.9), Tab. 3.3.

Breakpoints in proton energy spectrum (between 2 – 5 MeV) where the number of protons is steeply increased (see Fig. 3.12) are given by transverse dimensions of the target relative to the direction of propagation of the incident laser pulse. If the target had infinite transverse dimension (a situation similar to real experiments), the increase in the number of protons would never appear. Breakpoints in energies of protons are created on high-energy carbon front locations as demonstrated of Fig. 3.13. Naturally, there are no breakpoints in energy spectrum of carbon ions.

Fig. 3.13 also demonstrates that protons are accelerated more efficiently than  $C^{4+}$  ions because of their more favorable  $q/m$  ratio. Protons are shielding the field before carbon ions, thus, these ions cannot be accelerated to such high energies (per atomic mass unit) or, in other words, to such high velocities, than protons. Actually, the possibility of easy comparison of particle velocities squared is the reason why we use division by atomic mass unit  $u$ .

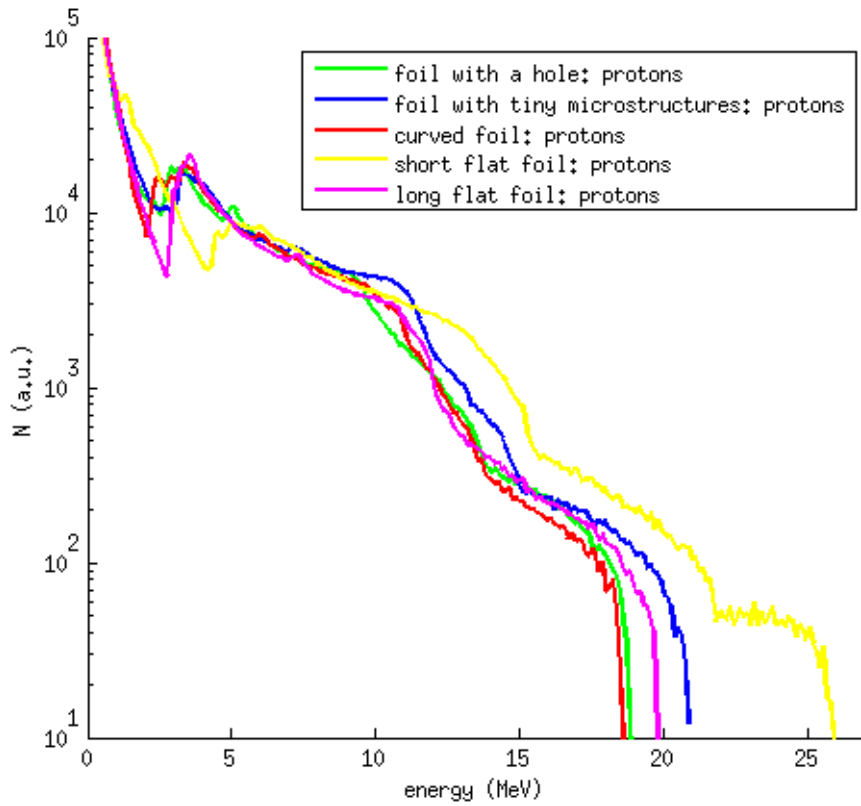


Figure 3.12: Energy spectrum of protons for foil with a hole on its rear side (green), foil with tiny microstructures on its rear side (blue), curved foil (red), short flat foil (yellow) and long flat foil (pink) at the end of simulation at  $t = 300$  fs; energetic spectrum covers only protons which are moving forward

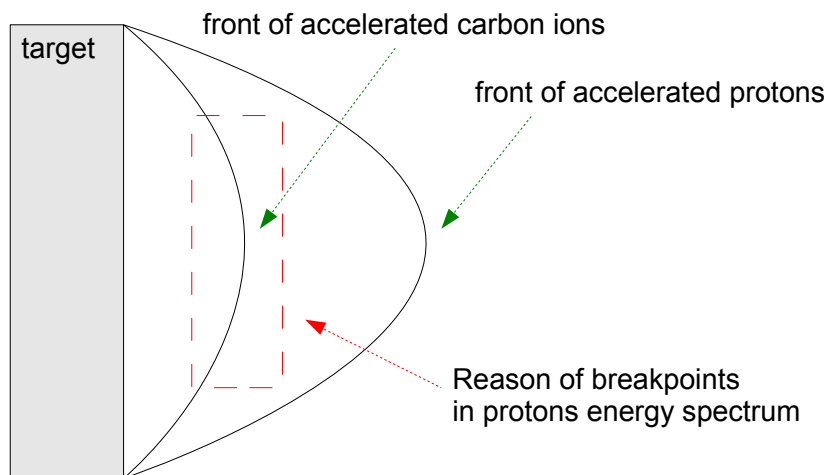


Figure 3.13: Illustration of the position of the front of accelerated protons and heavier ions; the most accelerated carbon ions are reason why breakpoints in proton energy spectrum are present

### 3.9 Energy balance

Absorption coefficient is equal to maximum kinetic energy after the interaction divided by the maximum energy of the electromagnetic field in the simulation domain before the interaction. It is important to take the value of maximum field energy at time when the whole laser pulse is present in the simulation area. Our conditions are satisfied for times  $t_{before} = 30$  fs and  $t_{after} = 300$  fs. Finally, the relation for absorption coefficient  $\kappa$  is then:

$$\kappa = \frac{W_{max}^{kin}(t_{after})}{W_{max}^{field}(t_{before})}, \quad (3.24)$$

where  $W_{max}^{kin}$  is maximum kinetic energy and  $W_{max}^{field}$  is maximum energy of laser (EM) field, same notations are used in Energy balance section 3.4.3.

Values of absorption coefficient  $\kappa$  for all targets are listed in Tab. 3.3.

type of target	flat long	flat short	curved	with a hole	with tiny microstructures
$\kappa$ [%]	29.4	28.4	27.0	28.3	29.9

Table 3.3: Values of absorption coefficient  $\kappa$  (3.24) for various target designs

Values of absorption coefficient do not diverse much ( $\sim 5\%$ ) in contrast to absorption coefficients obtained from simulations of flat and curved foil with comparable parameters [10] but irradiated at lower laser pulse intensity ( $4.5 \cdot 10^{19}$  Wcm $^{-2}$  instead of  $4.5 \cdot 10^{20}$  Wcm $^{-2}$ ). There, curved foil has  $\sim 1.4$  times greater absorption coefficient  $\kappa$  than flat foil (21.4% and 15.6%, respectively).

In the case of curved foil, the laser pulse is incident on the target surface at various angles in contrast to flat foil case in which the laser pulse is incident perpendicularly to the target surface, i.e. comes to the front side at zero angle. Electron heating mechanisms, such as Brunel vacuum heating [67], are inefficient when the laser pulse is incident at zero angle. On the other hand,  $\vec{j} \times \vec{B}$  heating [67] takes place also for normal incidence. Furthermore,  $\vec{j} \times \vec{B}$  heating applies successfully for much higher intensities than other heating mechanism, because in such relativistic cases magnetic field term in Lorentz force become bigger and bigger which corresponds to small differences between absorption coefficients (Tab. 3.3) and also to an apparent change in increasing/decreasing tendency of  $\kappa$ .

Moreover, effective intensity is smaller on the surface of curved foil as we can see from a simple geometry consideration (see Fig. 3.14): circumscribing the space by  $y_1, y_2$ , the corresponding laser pulse energy is absorbed by the small area  $ds_1$  (curved foil) and  $ds_2$  (flat foil), where curved foil area is obviously bigger. In short, the same amount of energy is absorbed by a larger surface (curved foil) and thus, the effective intensity is smaller even when the beam is relatively narrow compared to the size of the target. This can be one of the factors explaining the obtained results summarized in Tab. 3.3.

Energy balance displaying progress of total energy  $W_{tot}$ , total kinetic energy  $W_{kin}$ , field energy  $W_{field}$  and kinetic energies of protons  $W_{kin}^{p+}$ , carbon ions  $W_{kin}^{C^{4+}}$  and electrons  $W_{kin}^{e-}$  in time is depicted in Fig. 3.15 for the long flat foil. Energy variables are computed according to equations in section 3.4.3 and all of them use dimensionless magnetic and electric field  $\vec{B}'$ ,  $\vec{E}'$  (3.16).

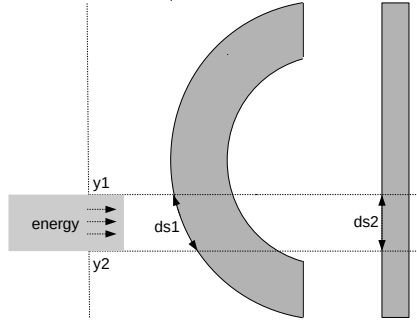


Figure 3.14: Geometric interpretation of effective intensity

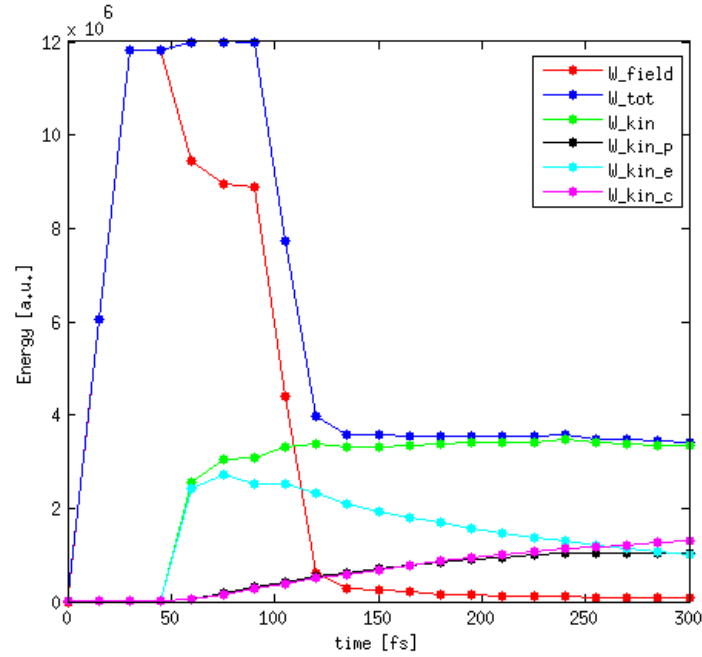


Figure 3.15: Energy balance for flat foil section; total energy  $W_{tot}$ , kinetic energy of all particles  $W_{kin}$ , field energy  $W_{field}$ , kinetic energy of protons  $W_{kin_p}$ , kinetic energy of electrons  $W_{kin_e}$  and kinetic energy of  $C^{4+}$  ions  $W_{kin_c}$

In Fig. 3.15, we can observe that laser energy  $W_{field}$  starts decreasing from 50 fs to 100 fs when energy of laser pulse is absorbed by electrons ( $W_{kin_e}$  rises). The most of the pulse is reflected from the target and from the time 100 fs is absorbed on the edge of simulation area. Then, kinetic energy of electrons  $W_{kin_e}$  is gradually transferred into proton kinetic energy  $W_{kin_p}$  and ion kinetic energy  $W_{kin_c}$  till the end of the simulation.

### 3.10 Phase space

The principle of TNSA mechanism and stages of acceleration process will be demonstrated in the case of long flat foil by the time evolution of the proton density and position in the phase space. Figure 3.16 shows proton density as well as proton velocity  $v_x$  dependent on  $x$ -dimension of phase space and it is plotted in six different times: 45 fs (before the interaction), 60 fs (when the laser pulse is starting to interact with the foil), 90 fs, 120 fs, 210 fs and 300 fs (the end of the simulation), respectively. In those plots, only small part of the target ( $1 \times 12 \mu\text{m}$ ) around the central axis (i.e. small center part taking area  $x \in \langle -5; 100 \rangle \mu\text{m}$  and  $y \in \langle -0.5; 0.5 \rangle \mu\text{m}$ ) is taken into account because the particles are accelerated mostly here.

In Fig. 3.16 a), the flat long target before any interaction with laser pulse is shown. Still, there are two tails at both sides of the target surface corresponding to very small expansion caused by thermal movement of the particles (in PIC simulations, macroparticles are initialized with nonzero thermal velocities in order to ensure numerical stability). In Fig. 3.16 b), we can see the moment when the laser pulse is starting to interact with only the front side of the target – this corresponds to a sharp peak at the beginning illustrating rapid increase in velocities of front target particles moving in forward direction. Actually, this phenomena matches the RPA acceleration concept where particles are accelerated from the front side by the radiation pressure to much more higher velocities, than those obtained via TNSA mechanism, and these protons nearly overtake protons from the foil rear side in the end. The small tails at the front and at rear side of the target correspond to early stage of TNSA mechanism; these tails grow a lot with acceleration time as we will see on the next pictures. In fact, RPA does not end after the interaction as it is demonstrated in Fig. 3.16 d) where TNSA scenario is applied as well as RPA which accelerates particles in some time to even higher energies than TNSA. Target Normal Sheath acceleration is characterized by smooth velocity increase on longer distance where particles are accelerated mainly from the rear side of the target in the forward direction, nevertheless also expansion from the front side in the backward direction (in phase plots shown as negative velocity) is present, see Fig. 3.16 d) – f). In Fig. 3.16 d) – f) we can observe two bunches – first one is formed by the faster ions accelerated from the front side (which is moving closer and closer to the rear side) via RPA and it can catch up the second bunch formed by ions accelerated via TNSA from the rear side. Over time, these bunches (i.e. speeds of accelerated ions) will become almost identical.

Furthermore, in Fig. 3.17 one can see the time evolution of proton density plot in five time steps. The foil is initially located from 0 to  $1 \mu\text{m}$  on the  $x$ -axis and expands into the vacuum. For comparison, the target before interaction (in time 45 fs; cyan line) is shown. After the interaction in 60 fs (start of the interaction between the target and the laser pulse corresponds to sharp increase in density at the target front), the target surface is pushed inwards and the whole target moves forward afterwards. This explains the bigger and bigger space shift between density curves with time.

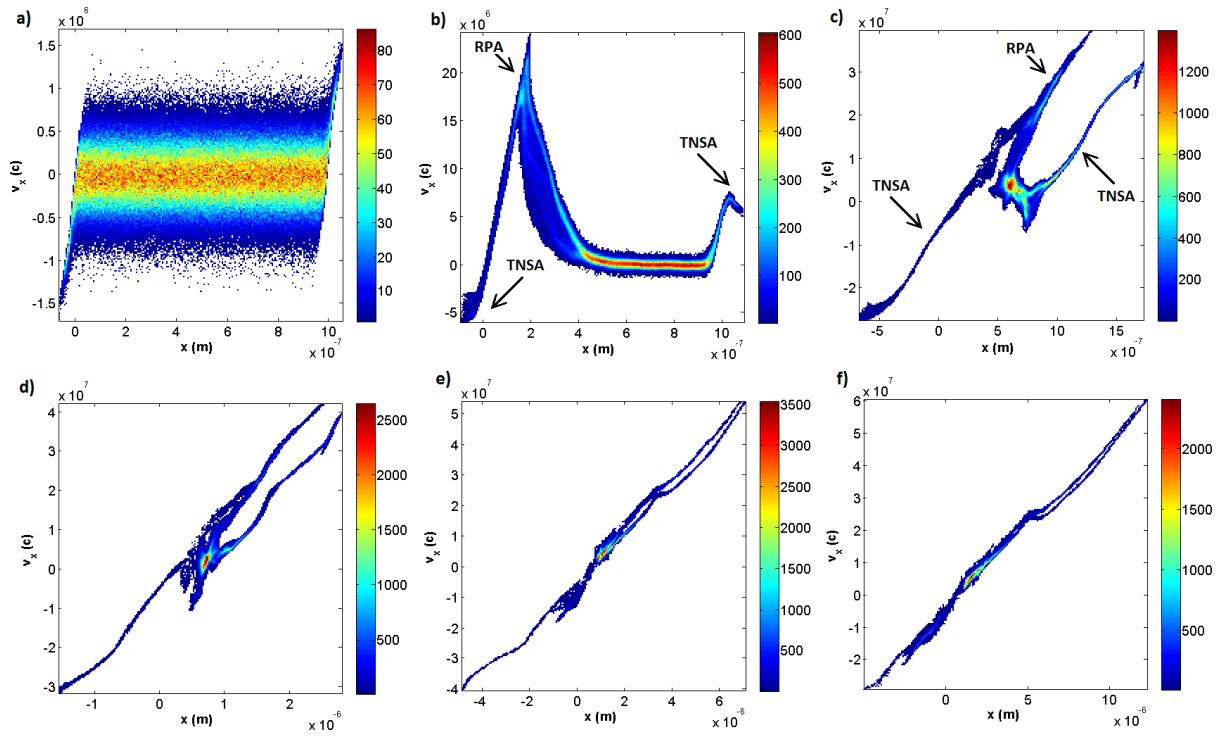


Figure 3.16: Time evolution of proton beam in phase space: a) 45 fs (before interaction), b) 60 fs (laser pulse is starting to interact with the target), c) 90 fs, d) 120 fs, e) 210 fs, f) 300 fs (end of the simulation); chosen area  $x \in \langle -5; 100 \rangle \mu\text{m}$  and  $y \in \langle -5.5; 5.5 \rangle \mu\text{m}$

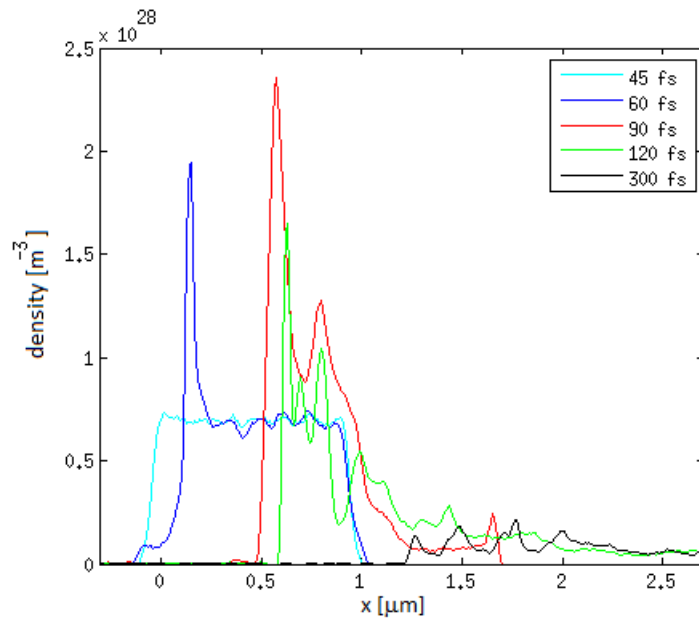


Figure 3.17: Time evolution of proton density, 45 fs (cyan), 60 fs (blue), 90 fs (red), 120 fs (green), 300 fs (black), target is  $1 \mu\text{m}$  wide and is located initially from  $0 \mu\text{m}$  to  $1 \mu\text{m}$

### 3.11 Fabrication of targets with microstructures and planned experiments

In general, it is hard to create plastic layers thinner than  $1\ \mu\text{m}$ , because plastic materials are not compact enough and, thus, grids are not suitable anymore. Nevertheless, for producing thin layers, silicon-nitride ( $\text{Si}_3\text{N}_4$ ) support *films*, with possible thickness even  $8\ \text{nm}$  [68], can be used. Particular silicon nitride thin films are produced e.g. by plasma enhanced chemical vapor deposition (PECVD) technique with low values of mechanical stress and high deposition rate [69]. PECVD is common dielectric thin film deposition technique and it uses, among others, as a structural layer for the fabrication of rigid membranes and other mechanical parts from nanometers to microns. Fabrication was performed with mixed frequency procedure varying the modulation of low and high frequency of RH power supply during the deposition, without changing the ratio of reaction gases [69].

Currently, a Laserlab experimental campaign is planned by our group at Lund test facility in Sweden. The main goal is to investigate experimentally different types of nano and micro structured targets to produce proton beams with low divergence, high charge, high energy, and homogeneous spatial profile. The experimental work can be divided in three main steps according to three different goals. Firstly, the number of accelerated protons (via TNSA regime), their maximum energy and their spatial distribution will be evaluate for  $\mu\text{m}$ -thick Mylar targets with polystyrene nano-spheres deposited on their front surface (where the laser interacts). The enhancement of both proton number and maximum energy is expected.

Secondly, the grating targets, i.e. one-dimensional micro-structures on the target rear side, will be used to control the emitted proton beam angular distribution and thus, reduce the proton beam divergence. Two-dimensional PIC simulations presented here helped to create the preliminary targets for the experiment, see 3.18. For now, the target list contains three foils with microstructures (i.e. gratings) on it rear side with gaps  $0.5\ \mu\text{m}$  (Fig. 3.19),  $1.0\ \mu\text{m}$  and  $2.0\ \mu\text{m}$ . For creating these targets a silicone nitride support film was used.

Lastly, the grating targets will also be tested in a reversed configuration (the gratings facing the incoming laser) to increase the laser absorption, thus the proton acceleration efficiency [70]. Moreover, complex targets containing both the nano-spheres (increase the proton beam charge, maximum energy and spatial homogeneity) and the micro-gratings (lower beam divergence) will be used.

The planned Lund experiment can show the proof-of-principle capability of controlling crucial proton beam parameters, such energy spread, beam divergence or particle number, only by improving the target fabrication and without using large conventional beam transport devices which is a huge advantage for future user applications.

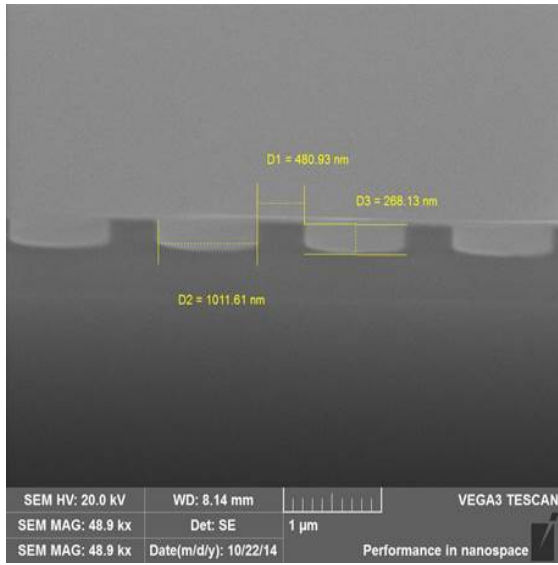


Figure 3.18: Side view on the target with periodic microstructures on its rear side designed and produced in Fondazione Bruno Kessler (FBK, Trento) based on PIC simulations presented here; (picture from scanning electron microscope)

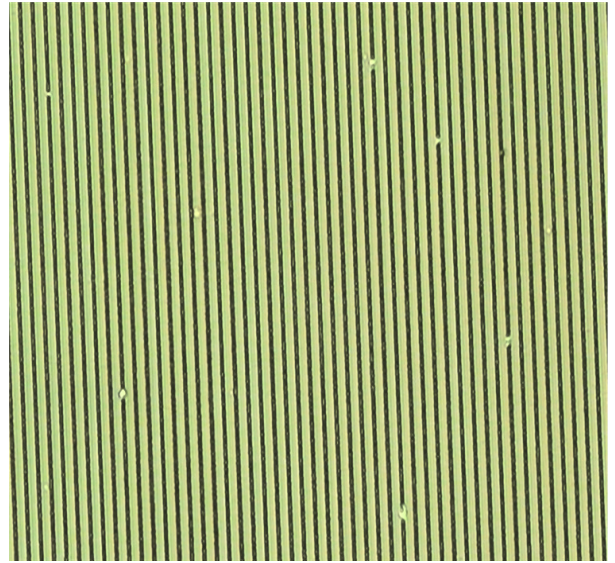


Figure 3.19: Target with grating with  $0.5 \mu\text{m}$  gaps designed and produced in Fondazione Bruno Kessler (FBK, Trento); (picture from the laser scanning microscope)

## Chapter 4

# Numerical simulations of proton trajectories in magnetic solenoid

The Matlab code which was developed in my bachelor thesis [9] and then modified with my research project [10] can compute the trajectory coordinates of a charged particle beam in a solenoid with given starting conditions for position and velocity coordinates. The present goal is to connect the obtained data from PIC simulations with the Matlab program, which has to be modified for this purpose.

### 4.1 Reduction of divergence by magnetic solenoid

Obtained data from PIC simulations discussed in previous section were further employed in postprocessing. We used two approaches for the divergence reduction – firstly, an aperture is placed behind the target and in front of a magnetic solenoid (see Fig. 4.1) and secondly, the divergence is controlled by optimizing the magnetic field inside the solenoid, i.e. by changing the current inside the coil.

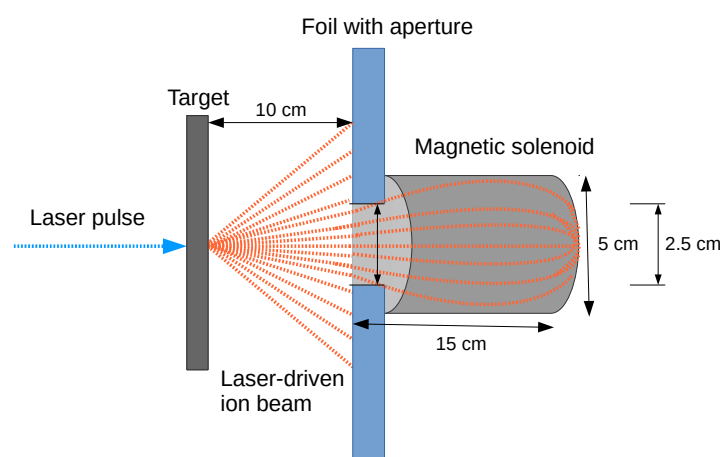


Figure 4.1: Scheme of the thought experiment explained in the text with aim to decrease the beam divergence

### 4.1.1 Applied code modifications

The PIC simulations were computed using the two-dimensional EPOCH code along with a Matlab program which computes particles trajectories in three dimensions, thus, the original numerical program had to be modified from 3D to 2D. The starting conditions set three parameters (in cylindrical coordinate system) to zero –  $\theta$ , its component of velocity  $v_\theta$  (i.e. there is no angular movement) and velocity in the direction of beam propagation  $v_z$ . The positions and momentum of the particles ( $r, v_r, v_z$  equivalent to  $y, v_y, v_x$  in Cartesian coordinate system used in the PIC simulations) are taken from PIC data and the suitable amount of particles (tens or hundreds instead of few millions in PIC) is chosen by placing an aperture in protons path and by application of three different energy intervals. Corresponding beam divergence were computed using  $x$  and  $y$  velocity components from geometrical interpretation.

### 4.1.2 Simulation parameters

In PIC simulations, we used several millions of particles, but we could hardly analyze such amount of particle trajectories. Therefore, only several sets with hundreds of particles with specific energies were taken into account in order to illustrate the effect of magnetic solenoid on the particle movement after their acceleration by laser. In the following calculations, the momentum components of accelerated protons originated from PIC simulations with long flat foil were employed.

Firstly, an aperture with diameter 2.5 cm was assumed 10 cm behind the target. Three energy intervals are set to 15.0 – 15.1 MeV, 10.0 – 10.05 MeV, 5.0 – 5.01 MeV and they are counting 116, 142 and 144 particles from PIC simulation, respectively.

Secondly, the divergence is further reduced by the magnetic solenoid which is installed directly behind the aperture. The coil is 15 cm long with diameter 5 cm and it has 1200 wire turns. The optimal value of wire current was set to 850 A (the corresponding magnetic field in the solenoid centre is 8.1 T) with the aim to decrease the beam divergence of  $\sim 15$  MeV protons as much as possible. Proton trajectories inside the solenoid are calculated from three differential equations of motion in a cylindrical coordinate system [9]:

$$m(\ddot{r} - r\dot{\theta}^2) = er\dot{\theta}B_z \quad \text{focusing,} \quad (4.1)$$

$$m(2\dot{r}\dot{\theta} + r\ddot{\theta}) = e(\dot{z}B_r - \dot{r}B_z) \quad \text{rotation,} \quad (4.2)$$

$$m\ddot{z} = -er\dot{\theta}B_r \quad \text{acceleration,} \quad (4.3)$$

where  $m$  is proton mass,  $r, \theta, z$  are cylindrical coordinates in space and  $B_r, B_z$  are two from three cylindrical components of magnetic field where  $B_\theta = 0$  because the field is axially symmetric, i.e. there is no angle dependence.

The trajectories are computed up to the end of the solenoid. In Fig. 4.1 the scheme of the thought experiment is demonstrated.

### 4.1.3 Results

The divergence of  $\sim 15$  MeV proton beam is compared in different stages of the system including the long flat target, the aperture and the magnetic solenoid in this order. In the first case, the results at the end of PIC simulations are taken into account. Those protons suggest the biggest divergence angle as expected (blue dot-dash line), see Fig. 4.2 and Tab. 4.1. The corresponding angular spectrum after the beam propagation through aperture is plotted

by the magenta dashed line in Fig. 4.2. Finally, the divergence angle is measured at the end of the magnetic solenoid after the beam goes through the aperture (which ensures that all the protons fly inside the coil) and the solenoid itself (green line). The results clearly demonstrate that the proton beam divergence can be reduced not only by various target designs, but also by the use of a magnetic solenoid. The divergence of  $\sim 15$  MeV proton beam is decreased from  $10.5^\circ$  to  $0.9^\circ$  after application of aperture and coil together, see Tab. 4.1. The total number of protons in the applied energy interval (15.0–15.1 MeV) was reduced from 235 particles (input from PIC; where only protons moving forward are taken) to 116 protons which pass through the aperture and enter the solenoid located directly behind the aperture, so no particle is reflected back or misses the solenoid. In general, the program is focused on computing particle trajectories and beam divergence; no recombination processes etc. are taken into account, so the total number of protons at the end of the solenoid remains the same as at its start. The total number of protons moving forward with all energies is  $\sim 3.370.000$  at the beginning.

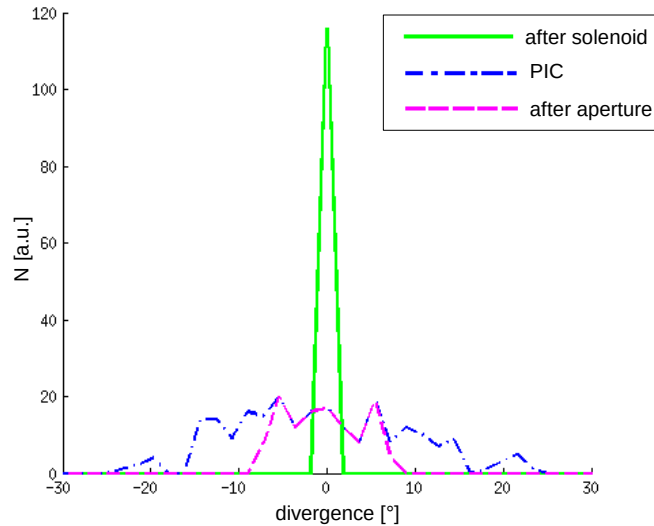


Figure 4.2: Comparison of angular distribution of proton bunch with energy from 15.0 MeV to 15.1 MeV obtained from PIC simulation (blue), after applying the aperture (magenta) and after passing through the magnetic solenoid with optimal value of wire current 850 A (green)

	half-angle divergence [°]
PIC	10.5
aperture	6.9
solenoid	0.9

Table 4.1: Comparison of divergence angle measured in FWHM of proton beam with energy from 15.0 MeV to 15.1 MeV: obtained from PIC simulation, after applying the aperture and after passing through the magnetic solenoid (when aperture is still taken into account)

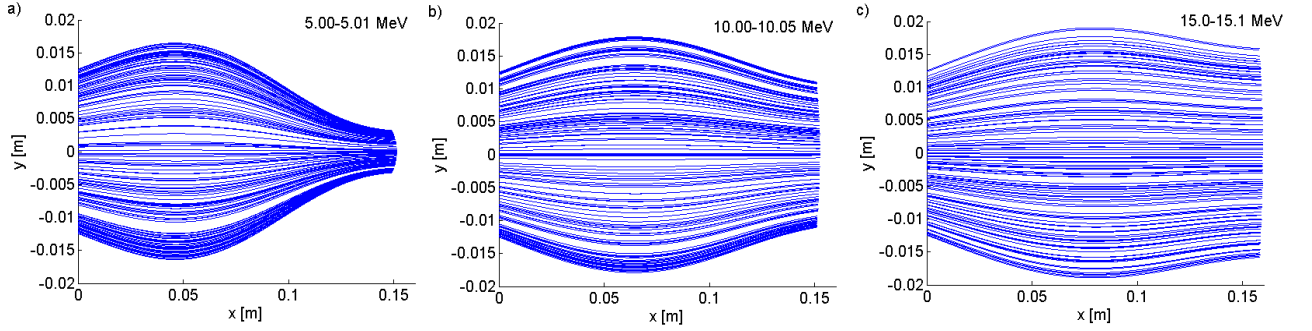


Figure 4.3: Trajectories of proton beam travelling through  $15 \times 5$  cm magnetic solenoid illustrating the beam divergence at the end of the coil; the wire current was set to 850 A; protons from PIC simulations within three different energy intervals are taken into account: (a) 5.0 – 5.01 MeV, (b) 10.0 – 10.05 MeV and (c) 15.0 – 15.1 MeV

Thus, the smallest divergence for protons with energy  $\sim 15$  MeV (the aperture is already applied) was found for a current of 850 A and corresponds to  $0.9^\circ$  half angle divergence in FWHM. Naturally, one value of wire current is the most suitable for only one energy for which it causes the highest decrease of divergence. In Fig. 4.3 we can observe proton trajectories not only with  $\sim 15$  MeV but also with  $\sim 5$  and  $\sim 10$  MeV, both having a larger divergence than  $\sim 15$  MeV protons ( $\sim 5$  and  $\sim 10$  MeV protons are forming a larger angle with the axis than  $\sim 15$  MeV protons which are nearly parallel to the x-axis). Although the values of divergence for less energetic protons are bigger, the corresponding beam is thinner at the end of the solenoid. In fact, the beams with high divergence are defocused behind the solenoid very rapidly. Actually, the comparison between angular distributions of different energy interval of simulated protons is shown in Fig. 4.4 and values of angular half angle divergence measured in FWHM are summarized in Tab. 4.2. These results demonstrate that divergence of  $\sim 15$  MeV proton beam is two times lower than divergence of  $\sim 10$  MeV beam and nearly four times lower than that of  $\sim 5$  MeV protons for a given current (i.e. magnetic field) in the coil.

Energy	half-angle divergence [ $^\circ$ ]
$\sim 15$ MeV	0.9
$\sim 10$ MeV	2.0
$\sim 5$ MeV	3.8

Table 4.2: Angular half-angle FWHM divergence for different energy intervals of proton beam, values correspond to Fig. 4.4

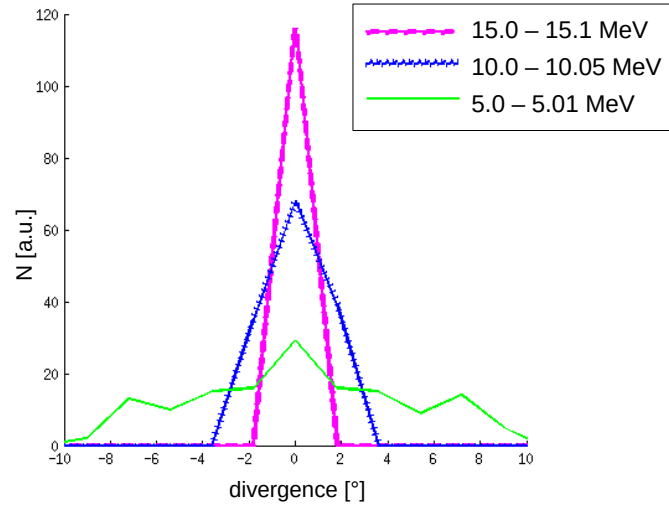


Figure 4.4: Angular distribution of protons after passing  $15 \times 5$  cm magnetic solenoid. The value of wire current is set to 850 A (which induces magnetic field 8.1 T inside the solenoid) in order to optimize the divergence of  $\sim 15$  MeV protons. Energy interval differ in range to obtain similar amount of particles in the simulation

# Summary and Conclusion

There are many applications of laser-driven ion beams for which having a low divergence is crucial. Various possibilities how to decrease the beam divergence are used. In this work, two basic approaches for the angular spread reduction of laser-accelerated ions were demonstrated. The first way is to use advanced target designs. We carried out Particle-in-cell (PIC) simulations for five different foil types including long and short flat foils, foil with tiny microstructures on its rear side, foil with a hole on its surface and curved target. Obtained results show that well-designed microstructures, i.e. a hole in the center of the target, can produce proton beam with the lowest divergence, namely  $\sim 9^\circ$ , while the second best result was obtained for the curved foil. Moreover, the particle beam accelerated from a curved foil has lower divergence compared to the beam from a flat foil. The maximum accelerated energies do not vary much for all target types except the short flat foil which reaches  $\sim 26$  MeV, i.e. nearly one third greater value than the other targets.

The second possibility for the reduction of angular spread of particles is to install small magnetic devices (in our case magnetic solenoid) into the beam path. The angular distribution of  $\sim 15$  MeV protons was calculated at the end of the PIC simulation behind the long flat target, after passing through 2.5 cm diameter aperture and through  $15 \times 5$  cm magnetic solenoid. The divergence of accelerated protons decreased from  $10.5^\circ$  after the acceleration stage to  $0.9^\circ$  after passing through the solenoid with wire current 850 A (corresponding to magnetic field inside the solenoid 8.1 T). This proves, that magnetic solenoid can be used to reduce divergence in a given energy interval.

This work is important for the implementation and optimization of future experiments at ELI-Beamlines and also for experiments which are planned in the near future at test facilities. Future work has to be carried out to find the best coupling between the type of target and the solenoid configuration with the main goal to increase the efficiency (total number of particles) of the beam transport system that is crucial for enhancing the deposited dose on a potential user sample. Also the parametric study of target's microstructures dimensions is being prepared with the aim to obtain the lowest divergence as possible. Mainly, we will focus on the ideal ratio between length of gaps and microstructures length as well as on the most favorable thickness of such microstructures while technical feasibility will be taken into account. Consequently, the cooperation with material scientists is expected. In the future, the coupling between microstructures both on rear and front side will be probably simulated and explored in subsequent experiments.

The question of divergence reduction is very wide and covers also the implementation of laser parameters which can be studied by PIC simulations. Naturally with more powerful lasers (i.e. with higher and higher intensities) new accelerating scenarios will appear and will have to be investigated more deeply.

# Bibliography

- [1] A Macchi, M Borghesi, and M Passoni. Ion acceleration by superintense laser-plasma interaction. *Reviews of Modern Physics*, 85(2):751, 2013.
- [2] KWD Ledingham, PR Bolton, N Shikazono, and C-M C Ma. Towards laser driven hadron cancer radiotherapy: A review of progress. *Applied Sciences*, 4(3):402–443, 2014.
- [3] JH Bin, WJ Ma, K Allinger, HY Wang, D Kiefer, S Reinhardt, P Hilz, K Khrennikov, S Karsch, XQ Yan, et al. On the small divergence of laser-driven ion beams from nanometer thick foils. *Physics of Plasmas (1994-present)*, 20(7):073113, 2013.
- [4] SN Chen, E d’Humières, E Lefebvre, L Romagnani, T Toncian, P Antici, P Audebert, E Brambrink, CA Cecchetti, T Kudyakov, et al. Focusing dynamics of high-energy density, laser-driven ion beams. *Physical review letters*, 108(5):055001, 2012.
- [5] J Limpouch, J Pšikal, O Klimo, J Vyskočil, J Proška, F Novotný, L Štolcová, and M Květoň. Laser ion acceleration: from present to intensities achievable at eli-beamlines. In *SPIE Optics+ Optoelectronics*, pages 878027–878027. International Society for Optics and Photonics, 2013.
- [6] M Nishiuchi, I Daito, M Ikegami, H Daido, M Mori, S Orimo, K Ogura, A Sagisaka, A Yogo, AS Pirozhkov, et al. Focusing and spectral enhancement of a repetition-rated, laser-driven, divergent multi-mev proton beam using permanent quadrupole magnets. *Applied Physics Letters*, 94(6):061107, 2009.
- [7] M Nishiuchi, AS Pirozhkov, H Sakaki, K Ogura, T Zh Esirkepov, T Tanimoto, M Kanasaki, A Yogo, T Hori, A Sagisaka, et al. Quasi-monochromatic pencil beam of laser-driven protons generated using a conical cavity target holder. *Physics of Plasmas (1994-present)*, 19(3):030706, 2012.
- [8] JS Green, NP Dover, M Borghesi, CM Brenner, FH Cameron, DC Carroll, PS Foster, P Gallegos, G Gregori, P McKenna, et al. Enhanced proton beam collimation in the ultra-intense short pulse regime. *Plasma Physics and Controlled Fusion*, 56(8):084001, 2014.
- [9] M Žáková. Manipulace a transport iontových paprskou řízených laserem. 2013.
- [10] M Žáková. *Reduction of angular divergence of laser-driven ion beams during their acceleration and transport*. FNSPE Departement of Physics, 2013.
- [11] P Kulhánek. *Úvod do teorie plazmatu*. AGA, 2011.

- [12] J Limpouch. Transparencies of lectures principles of plasma physics. <http://kfe.fjfi.cvut.cz/~limpouch/plazma/lecplaz.html>, 2012. online, accessed 01-09-2014.
- [13] J Pšikal. *Ion Acceleration in Small-size Targets by Ultra-intense Short Laser Pulses (Simulation and Theory)*. PhD thesis, Czech Technical University, 2009.
- [14] X Zhang, B Shen, X Li, Z Jin, F Wang, and M Wen. Efficient gev ion generation by ultraintense circularly polarized laser pulse. *Physics of Plasmas (1994-present)*, 14(12):123108, 2007.
- [15] O Klimo, J Pšikal, J Limpouch, and VT Tikhonchuk. Monoenergetic ion beams from ultrathin foils irradiated by ultrahigh-contrast circularly polarized laser pulses. *Physical Review Special Topics-Accelerators and Beams*, 11(3):031301, 2008.
- [16] KA Flippo, BM Hegelich, MJ Schmitt, CA Meserole, GL Fisher, DC Gautier, JA Cobble, R Johnson, S Letzring, J Schreiber, et al. Ultrashort-laser-produced heavy ion generation via target laser-ablation cleaning. In *Journal de Physique IV (Proceedings)*, volume 133, pages 1117–1122. EDP sciences, 2006.
- [17] BM Hegelich, B Albright, P Audebert, A Blazevic, E Brambrink, J Cobble, T Cowan, J Fuchs, JC Gauthier, C Gautier, et al. Spectral properties of laser-accelerated mid-zmev/u ion beams. *Physics of Plasmas (1994-present)*, 12(5):056314, 2005.
- [18] D Jung. *Ion acceleration from relativistic laser nano-target interaction*. PhD thesis, lmu, 2012.
- [19] TM Jeong and J Lee. Femtosecond petawatt laser. *Ann. Phys. (Berlin)*, 16, 2014.
- [20] BM Hegelich. *Acceleration of heavy ions to MeV/nucleon energies by ultrahigh-intensity lasers*. PhD thesis, lmu, 2002.
- [21] K Flippo, BM Hegelich, BJ Albright, L Yin, DC Gautier, S Letzring, M Schollmeier, J Schreiber, R Schulze, and JC Fernandez. Laser-driven ion accelerators: Spectral control, monoenergetic ions and new acceleration mechanisms. *Laser and Particle Beams*, 25(01):3–8, 2007.
- [22] TE Cowan, AW Hunt, TW Phillips, SC Wilks, MD Perry, C Brown, W Fountain, S Hatchett, J Johnson, MH Key, et al. Photonuclear fission from high energy electrons from ultraintense laser-solid interactions. *Physical review letters*, 84(5):903, 2000.
- [23] B Qiao, S Kar, M Geissler, Paul Gibbon, M Zepf, and M Borghesi. Dominance of radiation pressure in ion acceleration with linearly polarized pulses at intensities of  $10^{21}$  w cm<sup>-2</sup>. *Physical review letters*, 108(11):115002, 2012.
- [24] A Macchi, S Veghini, and F Pegoraro. "Light sail" acceleration revisited. *arXiv preprint arXiv:0905.2068*, 2009.
- [25] L Yin, BJ Albright, BM Hegelich, and JC Fernández. Gev laser ion acceleration from ultrathin targets: The laser break-out afterburner. *Laser and Particle Beams*, 24(02):291–298, 2006.

- [26] L Yin, BJ Albright, BM Hegelich, KJ Bowers, KA Flippo, TJT Kwan, and JC Fernández. Monoenergetic and gev ion acceleration from the laser breakout afterburner using ultrathin targets. *Physics of Plasmas (1994-present)*, 14(5):056706, 2007.
- [27] BM Hegelich, I Pomerantz, L Yin, HC Wu, D Jung, BJ Albright, DC Gautier, S Letzring, S Palaniyappan, R Shah, et al. Laser-driven ion acceleration from relativistically transparent nanotargets. *New Journal of Physics*, 15(8):085015, 2013.
- [28] D Jung, BJ Albright, L Yin, DC Gautier, R Shah, S Palaniyappan, S Letzring, B Dromey, HC Wu, T Shimada, et al. Beam profiles of proton and carbon ions in the relativistic transparency regime. *New Journal of Physics*, 15(12):123035, 2013.
- [29] L Yin, BJ Albright, KJ Bowers, D Jung, JC Fernández, and BM Hegelich. Three-dimensional dynamics of breakout afterburner ion acceleration using high-contrast short-pulse laser and nanoscale targets. *Physical review letters*, 107(4):045003, 2011.
- [30] Q Dong and J Zhang. Vacuum heating of solid target irradiated by femtosecond laser pulses. *Science in China Series G: Physics, Mechanics and Astronomy*, 46(1):71–77, 2003.
- [31] M Roth, E Brambrink, P Audebert, M Basko, A Blazevic, R Clarke, J Cobble, TE Cowan, J Fernandez, J Fuchs, et al. Laser accelerated ions in icf research prospects and experiments. *Plasma physics and controlled fusion*, 47(12B):B841, 2005.
- [32] T Zh Esirkepov, SV Bulanov, K Nishihara, T Tajima, F Pegoraro, VS Khoroshkov, K Mima, H Daido, Y Kato, Y Kitagawa, et al. Proposed double-layer target for the generation of high-quality laser-accelerated ion beams. *Physical review letters*, 89(17):175003, 2002.
- [33] DT Offermann, KA Flippo, J Cobble, MJ Schmitt, SA Gaillard, T Bartal, DV Rose, DR Welch, M Geissel, and M Schollmeier. Characterization and focusing of light ion beams generated by ultra-intensely irradiated thin foils at the kilojoule scale a). *Physics of Plasmas (1994-present)*, 18(5):056713, 2011.
- [34] T Toncian, M Borghesi, J Fuchs, E d’Humières, P Antici, P Audebert, E Brambrink, CA Cecchetti, A Pipahl, L Romagnani, et al. Ultrafast laser-driven microlens to focus and energy-select mega-electron volt protons. *Science*, 312(5772):410–413, 2006.
- [35] S Kar, K Markey, PT Simpson, C Bellei, JS Green, SR Nagel, S Kneip, DC Carroll, B Dromey, L Willingale, et al. Dynamic control of laser-produced proton beams. *Physical review letters*, 100(10):105004, 2008.
- [36] T Burris-Mog, K Harres, F Nürnberg, S Busold, M Bussmann, O Deppert, G Hoffmeister, M Joost, M Sobiella, A Tauschwitz, et al. Laser accelerated protons captured and transported by a pulse power solenoid. *Physical Review Special Topics-Accelerators and Beams*, 14(12):121301, 2011.
- [37] TE Cowan, J Fuchs, H Ruhl, A Kemp, P Audebert, M Roth, R Stephens, I Barton, A Blazevic, E Brambrink, et al. Ultralow emittance, multi-mev proton beams from a laser virtual-cathode plasma accelerator. *Physical review letters*, 92(20):204801, 2004.

- [38] TE Cowan, U Schramm, T Burris-Mog, F Fiedler, SD Kraft, K Zeil, M Baumann, M Bussmann, W Enghardt, K Flippo, et al. Prospects for and progress towards laser-driven particle therapy accelerators. In *ADVANCED ACCELERATOR CONCEPTS: 14th Advanced Accelerator Concepts Workshop*, volume 1299, pages 721–726. AIP Publishing, 2010.
- [39] V Kumar. Understanding the focusing of charged particle beams in a solenoid magnetic field. *American Journal of Physics*, 77(8):737–741, 2009.
- [40] Asian Regional Team for ILC Accelerator Development. A batch of quadrupole magnets built for atf2. <http://lcdev.kek.jp/photos/20060330Di/20060330di-043.html>, 2006. online, accessed 12-04-2014.
- [41] J Psikal, VT Tikhonchuk, J Limpouch, AA Andreev, and AV Brantov. Ion acceleration by femtosecond laser pulses in small multispecies targets. *Physics of Plasmas (1994-present)*, 15(5):053102, 2008.
- [42] SV Bulanov and VS Khoroshkov. Feasibility of using laser ion accelerators in proton therapy. *Plasma Physics Reports*, 28(5):453–456, 2002.
- [43] V Malka, S Fritzler, E Lefebvre, E d’Humières, R Ferrand, G Grillon, C Albaret, S Meyroneinc, JP Chambaret, A Antonetti, et al. Practicability of protontherapy using compact laser systems. *Medical physics*, 31(6):1587–1592, 2004.
- [44] PK Patel, AJ Mackinnon, MH Key, TE Cowan, ME Foord, M Allen, DF Price, H Ruhl, PT Springer, and R Stephens. Isochoric heating of solid-density matter with an ultrafast proton beam. *Phys. Rev. Lett.*, 91:125004, Sep 2003.
- [45] JC Fernández, BJ Albright, FN Beg, ME Foord, BM Hegelich, JJ Honrubia, M Roth, RB Stephens, and L Yin. Fast ignition with laser-driven proton and ion beams. *Nuclear Fusion*, 54(5):054006, 2014.
- [46] M Roth, TE Cowan, MH Key, SP Hatchett, C Brown, W Fountain, J Johnson, DM Pennington, RA Snavely, SC Wilks, et al. Fast ignition by intense laser-accelerated proton beams. *Physical Review Letters*, 86(3):436, 2001.
- [47] Eli-beamlines project. <http://www.eli-beams.eu/>, 2011. online, accessed 17-02-2015.
- [48] D Margarone. Ion acceleration by fs lasers and potential applications. [http://www.eli-beams.eu/wp-content/uploads/2013/11/Margarone\\_ion\\_acceleration\\_by\\_fs\\_lasers.pdf](http://www.eli-beams.eu/wp-content/uploads/2013/11/Margarone_ion_acceleration_by_fs_lasers.pdf), 2013. online, accessed 17-02-2015.
- [49] M Carpinelli and GAP Cirrone. Elimed - medical and multidisciplinary applications at eli-beamlines. <https://agenda.infn.it/getFile.py/access?contribId=46&resId=0&materialId=slides&confId=6836>, 2014. online, accessed 17-02-2015.
- [50] GAP Cirrone. Hadrontherapy in the ocular melanoma tumor treatment: Experience from the first italian protontherapy center. <http://pablocirrone.wikispaces.com/file/view/Medicine-Talks+on+Hadrontherapy-Scientific+English\2.pdf>, 2012. online, accessed 19-03-2015.

- [51] V Ullmann. Fyzika a nukleární medicína - braggův pík. <http://astronuklfyzika.cz/JadRadFyzika6.htm>, 2013. online, accessed 12-12-2014.
- [52] Particle therapy co-operative group - a non-profit organisation for those interested in proton, light ion and heavy charged particle radiotherapy. <http://www.ptcog.ch/>, 2013. online, accessed 08-12-2014.
- [53] V Ullmann. Biologické účinky ionizujícího záření. <http://astronuklfyzika.cz/RadiacniOchrana.htm#2>, 2013. online, accessed 01-05-2014.
- [54] O Klimo. Physics of inertial fusion. <http://pi.fjfi.cvut.cz/html/joomla/index.php/en/vyuka/fyzika-inercialni-fuze>, 2014. online, accessed 01-11-2014.
- [55] T Bartal, ME Foord, C Bellei, MH Key, KA Flippo, SA Gaillard, DT Offermann, PK Patel, LC Jarrott, DP Higginson, et al. Focusing of short-pulse high-intensity laser-accelerated proton beams. *Nature Physics*, 8(2):139–142, 2012.
- [56] ME Foord, T Bartal, C Bellei, M Key, K Flippo, RB Stephens, PK Patel, HS McLean, LC Jarrott, MS Wei, et al. Proton trajectories and electric fields in a laser-accelerated focused proton beam. *Physics of Plasmas (1994-present)*, 19(5):056702, 2012.
- [57] University of Rochester. Laboratory for laser energetics. [http://www.lle.rochester.edu/quick\\_shots/#](http://www.lle.rochester.edu/quick_shots/#), 2014. online, accessed 20-01-2015.
- [58] BM Hegelich, BJ Albright, J Cobble, K Flippo, S Letzring, M Paffett, H Ruhl, J Schreiber, RK Schulze, and JC Fernandez. Laser acceleration of quasi-monoenergetic mev ion beams. *Nature*, 439(7075):441–444, 2006.
- [59] NA Krall, AW Trivelpiece, and RA Gross. Principles of plasma physics. *American Journal of Physics*, 41(12):1380–1381, 1973.
- [60] SA Ledvina, Y-J Ma, and E Kallio. Modeling and simulating flowing plasmas and related phenomena. *Space science reviews*, 139(1-4):143–189, 2008.
- [61] D Tskhakaya. The particle-in-cell method. In *Computational Many-Particle Physics*, pages 161–189. Springer, 2008.
- [62] CHK Birdsall and AB Langdon. *Plasma Physics Via Computer Simulation*. CRC Press, 2005.
- [63] CH Brady. The university of warwick: Centre for scientific computing - portfolio. [http://www2.warwick.ac.uk/fac/sci/csc/people/computingstaff/chris\\_brady/](http://www2.warwick.ac.uk/fac/sci/csc/people/computingstaff/chris_brady/), 2012. online, accessed 03-04-2014.
- [64] CESNET. Metacentrum. <http://www.metacentrum.cz/>, 2012. online, accessed 05-04-2014.
- [65] R Lichters, R EW Pfund, and J Meyer-ter Vehn. Lpic++. a parallel one-dimensional relativistic electromagnetic particle-in-cell code for simulating laser-plasma-interaction. Technical report, Max-Planck-Institut fuer Quantenoptik, Garching (Germany), 1997.

- [66] YJ Gu, Z Zhu, XF Li, Q Yu, S Huang, F Zhang, Q Kong, and S Kawata. Stable long range proton acceleration driven by intense laser pulse with underdense plasmas. *Physics of Plasmas (1994-present)*, 21(6):063104, 2014.
- [67] P Mulser and D Bauer. *High Power Laser-Matter Interaction*, volume 238. Springer Science & Business Media, 2010.
- [68] INC. Microscopy Products for Science TED PELLA and Industry. Pelco silicon nitride support films for tem. [http://www.tedpella.com/grids\\_html/silicon-nitride.htm](http://www.tedpella.com/grids_html/silicon-nitride.htm), 2015. online, accessed 18-02-2015.
- [69] A Picciotto, A Bagolini, P Bellutti, and M Boscardin. Influence of interfaces density and thermal processes on mechanical stress of pecvd silicon nitride. *Applied Surface Science*, 256(1):251–255, 2009.
- [70] T Ceccotti, V Floquet, A Sgattoni, A Bigongiari, O Klimo, M Raynaud, C Riconda, A Heron, F Baffigi, L Labate, et al. Evidence of resonant surface-wave excitation in the relativistic regime through measurements of proton acceleration from grating targets. *Physical review letters*, 111(18):185001, 2013.